



Superelastic shape memory alloy cables: Part II – Subcomponent isothermal responses

Benjamin Reedlunn^{a,*}, Samantha Daly^{b,c}, John Shaw^d

^a Sandia National Laboratories, P.O. Box 5800, Albuquerque, NM 87185, USA

^b University of Michigan, Dept. of Mechanical Engineering, 2350 Hayward St., Ann Arbor, MI 48109, USA

^c University of Michigan, Dept. of Materials Science and Engineering, 2300 Hayward St., Ann Arbor, MI 48109, USA

^d University of Michigan, Dept. of Aerospace Engineering, 1320 Beal Ave., Ann Arbor, MI 48109, USA

ARTICLE INFO

Article history:

Received 8 June 2012

Received in revised form 19 January 2013

Available online 6 April 2013

Keywords:

Shape Memory Alloys

NiTi

Nitinol

Cables

Wire rope

Digital image correlation

Infrared thermography

Tensile testing

Superelasticity

ABSTRACT

This paper constitutes the second part of our experimental study of the thermo-mechanical behavior of superelastic NiTi shape memory alloy cables. Part I introduced the fundamental, room temperature, tensile responses of two cable designs (7×7 right regular lay, and 1×27 alternating lay). In Part II, each cable behavior is studied further by breaking down the response into the contributions of its hierarchical subcomponents. Selected wire strands were extracted from the two cable constructions, and their quasi-static tension responses were measured using the same experimental setup of Part I. Consistent with the shallow wire helix angles in the 7×7 construction, the force–elongation responses of the core wire, 1×7 core strand and full 7×7 cable were similar on a normalized basis, with only a slight decrease in transformation force plateaus and slight increase in plateau strains in this specimen sequence. By contrast, each successive 1×27 component (1×6 core strand, 1×15 strand, and full cable) included an additional outer layer of wires with a larger number of wires, greater helix radius, and deeper helix angle, so the normalized axial load responses became significantly more compliant. Each specimen in the sequence also exhibited progressively larger strains at failure, reaching 40% strain in the full 1×27 cable.

Stress-induced phase transformations involved localized strain/temperature and front propagation in all of the tested 7×7 components but none of the 1×27 components aside from the 1×27 core wire. Stereo digital image correlation measurements revealed finer features within a global transformation front of the 1×7 core strand than the 7×7 cable, consisting of a staggered pattern of individual wire fronts that moved in lock-step during elongation. Although the 1×27 multi-layer strands exhibited temperature/strain localizations in a distributed pattern during transformations, the localizations did not propagate and their cause was traced back to contact indentations (stress concentrations) arising from the cable's fabrication. The normalized axial torque responses of the multi-layer 1×27 components during transformation were distinctly non-monotonic and complex, due to the alternating handedness of the layers. Force and torque contributions of individual wire layers were deduced by subtracting 1×27 component responses, which helped to clarify the transformation kinetics within each layer and explain the unusual force and torque undulations seen in the 1×27 cable response of Part I.

© 2013 Elsevier Ltd. All rights reserved.

1. Introduction

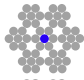
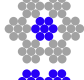
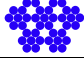
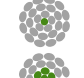


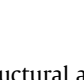
This is the second article of our two-part series exploring the tensile response of superelastic shape memory alloy (SMA) cables. Part I (Reedlunn et al., 2013) reviewed the construction of typical structural cables (wire ropes) and described how SMA wire in cable form combines the attractive properties of structural cables (redundant load carrying and spooling for compact packing) with the adaptive characteristics of SMAs (shape memory and super-

elasticity). Besides these independent features, the combination has additional synergetic advantages (tailorable structural performance, reduced thermal lag, and ease of manufacture for large force applications) that make a characterization study of SMA cables of both scientific and engineering interest. Two SMA cable designs, a 7×7 right regular lay and a 1×27 alternating lay, constructed of superelastic NiTi wires (as received from Ft. Wayne Metals Research) were described and characterized. A custom experimental setup, involving infrared (IR) thermography and stereo digital image correlation (DIC), examined the isothermal, superelastic responses of the two designs. The two cable designs exhibited quite different thermomechanical responses, spanning a range of superelastic behaviors, each of which might be advanta-

* Corresponding author. Tel.: +1 505 284 9677.

E-mail addresses: breedlu@sandia.gov (B. Reedlunn), samdaly@umich.edu (S. Daly), jshaw@umich.edu (J. Shaw).

Table 1
Specimen components from two cable designs and experimental and geometric parameters

Cable	Specimen	Icon	A_0 (mm ²)	J_0/R (mm ³)	Exp ID	L (mm)	L_e (mm)	$\dot{\delta}/L$ (s ⁻¹)
7 × 7	Core wire		0.059	4.083×10^{-3}	W1b	76.04	49.55	$\pm 1 \times 10^{-5}$
	1 × 7 Core strand		0.416	7.486×10^{-2}	S1a	75.93	50.17	$\pm 1 \times 10^{-5}$
	7 × 7 Cable		2.910	1.547×10^0	C1c	74.85	49.92	$\pm 1 \times 10^{-5}$
1 × 27	Core wire		0.040	2.266×10^{-3}	W2b	74.67	49.05	$\pm 1 \times 10^{-4}$
	1 × 6 Core strand		0.241	3.475×10^{-2}	S2a	75.05	49.70	$\pm 1 \times 10^{-4}$
	1 × 15 multi-layer		0.602	1.555×10^{-1}	M2a	75.09	49.88	$\pm 1 \times 10^{-4}$
	1 × 27 Cable		1.083	3.947×10^{-1}	C2d	75.21	49.21	$\pm 1 \times 10^{-4}$

geous depending on the intended structural application. The 7 × 7 cable performed similar to forty-nine NiTi wires pulled in parallel, and stress-induced transformations (both $A \rightarrow M^+$ during loading and $M^+ \rightarrow A$ during unloading) involved propagating transformation fronts as typically seen in straight NiTi wires. On the other hand, the 1 × 27 cable exhibited a significantly more compliant response, no propagating transformation fronts, and an intriguing axial torque response. In addition, the cyclic responses of the two designs were quite different, with less severe shakedown generally occurring in the 1 × 27 cable.

While Part I introduced the two designs by comparing their baseline performance, it raised a number of questions, especially for the 1 × 27 design. Here in Part II, we focus again on the same two cable designs and explore the isothermal response of selected subcomponents excised from each cable construction in an effort to explain the observed behavior of the full cables. It is also worthwhile to characterize the underlying components as a matter of scientific curiosity, and for the simple reason that certain applications may utilize the individual cable components as structural elements in their own right. The intended scope of this article is largely experimental and descriptive. For now, we leave the interesting topic of detailed structural modeling for future work and confine ourselves to simple analyses as needed to explain observed phenomena.

This article is organized as follows. Section 2 provides a summary of the experimental scope, focusing on the room temperature superelastic behavior of individual components at nearly isothermal elongation rates. Section 2 also provides further details on the geometry of the helical wires used in the cable designs. Section 3 provides a comparison of responses of three selected components in the 7 × 7 design, and provides experimental results showing further detail and new features of propagating transformation fronts in the straight core wire and the 1 × 7 core strand. Section 4 provides experimental responses of four selected components of the 1 × 27 construction, which help to explain the overall enhanced compliance of the full cable, the lack of localized self heating/cooling, the multi-knee force response, and the interesting “stair-step” torque response. Section 4 also provides a breakdown of the individual layer-by-layer responses, deduced by subtracting the components’ measured force and torque responses from one another.

2. Experimental scope & specimen details

The 7 × 7 × 0.275 mm and 1 × 27 × 0.226 mm cable designs, and their selected components used in this experimental study, are shown in Table 1. All specimens came from the same two cable lots utilized in Part I, and when necessary, the cables were disassembled to extract individual components for testing. The components shown in Table 1 are the set of nominally straight specimens that could be excised from the full cables: three for the 7 × 7 cable and four for the 1 × 27 cable. (All other possible components involved helical elements that would be much more challenging to test experimentally.) The experiments on the straight core wires and the full cables were presented in Part I; here we have added the intermediate components to study the complete hierarchy in the respective cable constructions. As before, specimens were lightly painted with a specular pattern to allow DIC measurements and to increase the emissivity of the surface for IR imaging, and reflective tags were attached to allow laser extensometry.

The same experimental setup as in Part I was utilized for the experiments presented in this paper. All experiments were performed on new, dry specimens in room temperature air. The lower grip was held fixed and the upper grip was displaced upward by a mechanical testing machine to stretch the specimen under elongation control at constant, slow ramp rates ($\dot{\delta}/L$) while monitoring the axial load. The grips rigidly clamped the specimen at its ends to enforce zero-rotation boundary conditions, and the resultant axial reaction torque was measured using a torque cell. In certain cases, stereo DIC was performed to measure the strain field evolution (in a restricted field of view) and infrared (IR) imaging was performed to measure the temperature field transients. Mechanical responses are presented in terms of the normalized axial load (P/A_0 , axial force per reference area) and normalized axial torque ($M_z R/J_0$, axial moment times outer radius per reference torsion constant). The chosen reference area (A_0) and reference torsion constant (J_0/R) were defined in Section 5 of Part I, and values are provided for each component being examined in Table 1. Sections 3 and 4 will present the respective experimental results and analyses of the component responses for the two cable types, 7 × 7 and 1 × 27. Responses are generally plotted either against the laser extensometer (LE) gage strain (δ_e/L_e) or time (t).

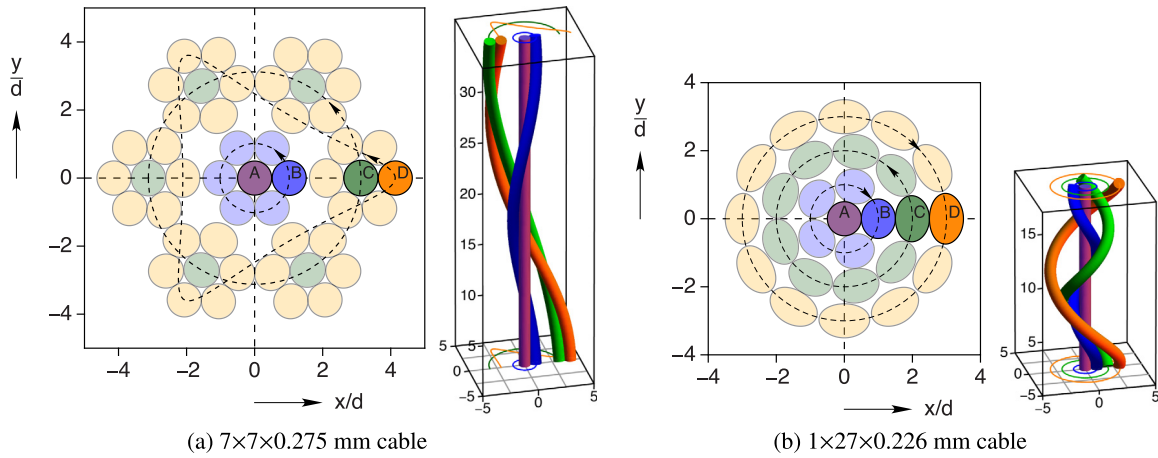


Fig. 1. Cross-section ($z = 0$) schematics and isometric views of the four wire types (A, B, C, D) with dimensions normalized by the wire diameter (d).

Fig. 1 provides a closer look at the geometry of individual wires in the 7×7 and 1×27 constructions. The 7×7 cable (Fig. 1(a)) is a multi-strand construction that includes one straight core strand and six outer helical strands. Each strand, in turn, consists of a central wire and six outer wires wound about it. Based on their geometry, we classify the wires into four groups (A, B, C, D) as indicated in the figure. The dashed lines in the cross-sections are projections of the trajectories of each wire type as it extends along the cable axis (z -axis), and an isometric view of each wire type is shown on the right. Geometric parameters for each wire type in each cable design are provided in Table 2. The reference helix angle to the cable axis (z -axis) is α_0 , the mean radius to wire centerline is r_0 , the reference axial pitch is p_0 , and the wire diameter is d . Wire A is the single straight core wire that runs along the centerline of the cable (z -axis). Wire type B is one of six helical wires wound in a right-hand sense around Wire A. Wire types A and B comprise the 1×7 core strand. Wire types C and D comprise the six outer helical strands. Wire C is one of six central wires of the outer helical strands, and it traverses a simple right-hand helix about the core strand. Wire D is the most prevalent wire type (36 of the 49 wires). It traverses a second-order helix, wrapping three left-hand turns about wire C for each right-hand turn of wire C about the z -axis, so two values for p_0 are given in Table 2 for wire D. The first ($p_0/d = 20.7$) is the pitch of wire D about wire C, while the second ($p_0/d = 62.2$) is the same pitch as wire C. The angle to the global cable axis in wire D varies from about 6° at its outermost point in the cable to about 28° (by calculation) at its innermost point adjacent to the core strand. These values should be treated as approximate, since the geometry has been idealized somewhat by assuming integer values of r_0/d . This is not strictly geometrically correct if one accounts for curvature effects on the projected wire sections, which can be seen upon close inspection of the true

projections in Fig. 1(a) where wires of different types do not quite touch. The drawing process used to make the cable, however, likely did not preserve this exact geometry either, as wires settled/deformed against one another.

The 1×27 cable's construction is significantly different from the 7×7 cable's construction, as shown in Fig. 1(b). The 1×27 cable is a single (multi-layered) strand, but it also has four wire types (A, B, C, D). In this case wires B, C, and D are all simple (first-order) helices in a left/right/left-hand lay. The respective helix angles are $(-30.4^\circ, 42.5^\circ, -47.9^\circ)$, which are larger in magnitude than the helical wires in the 7×7 cable. These values, along with other parameters provided in Table 2, reflect the exact (idealized) geometry shown in Fig. 1(b). Unlike the 7×7 cable, the different wire types touch each other radially one wire diameter apart, and a small gap exists circumferentially between wires of the same type. Again, however, one should recognize that the drawing process used in the cable's fabrication likely disturbed this geometry somewhat by wire settling/Hertzian contact.

3. Isothermal responses of the 7×7 cable components

The mechanical responses of the three selected components of the 7×7 cable exhibit similar superelastic responses when the axial load is normalized by the individual reference cross-sectional areas, as shown in Fig. 2. All three experiments were performed at the very slow rate of $\dot{\delta}/L = \pm 1 \times 10^{-5} \text{ s}^{-1}$ to achieve isothermal conditions and compare the fundamental, quasi static superelastic responses. Consistent with our previous observations in Part I, each component from the 7×7 cable behaves approximately as a bundle of straight wires loaded in parallel. Some quantitative differences do exist, however, and a few trends are apparent. Overall,

Table 2
Geometric parameters of the four wire types in the 7×7 and 1×27 cables, including number of wires, reference helix angle (α_0), normalized mean helix radius (r_0/d), and normalized pitch (p_0/d).

Cable type	Wire type	Number of wires	α_0	r_0/d	p_0/d
7 × 7	A	1	0°	0	NA
	B	6	11.3°	1	31.6
	C	6	16.9°	3	62.2
	D	36	5.6° to 28.2°	2 to 4	20.7, 62.2
1 × 27	A	1	0°	0	NA
	B	5	-30.4°	1	10.7
	C	9	42.5°	2	13.7
	D	12	-47.9°	3	17.0

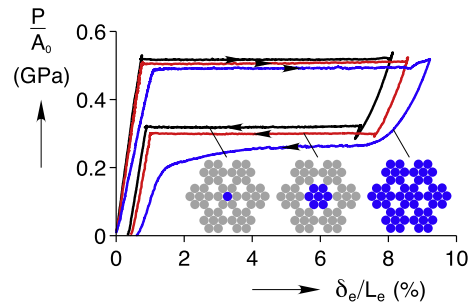


Fig. 2. Comparison of isothermal ($\dot{\delta}/L = \pm 1 \times 10^{-5} \text{ s}^{-1}$) normalized force-LE strain responses of $7 \times 7 \times 0.275$ mm components: straight core wire (Exp. W1b), 1×7 core strand (Exp. S1a), and full 7×7 cable (Exp. C1c).

a monotonic progression exists in the response curves, from the core wire, to the 1×7 core strand, to the full 7×7 cable. The upper load plateaus move downward slightly, the lower unload plateaus move downward to a greater extent, and the extent of the plateau strains increase somewhat. Note that each specimen was taken to a slightly different maximum strain (8.12%, 8.57%, and 9.21%), where unloading commenced just after the termination of the upper load plateau. The responses of the core wire and core strand are quite similar, with nearly identical initial elastic modulus (prior to $A \rightarrow M^+$) and both exhibiting distinct load plateaus during both $A \rightarrow M^+$ (loading) and $M^+ \rightarrow A$ (unloading) transformations. This is not surprising, since its straight core wire contributed $1/7$ of A_0 and the other six outer wires have relatively small helix angles (11.6°) to the loading axis. This means that all wires are loaded predominantly in direct tension, with only a very small bending and torsion contribution. The full 7×7 cable has a load plateau during $A \rightarrow M^+$, but a less distinct one during $M^+ \rightarrow A$, as well as a larger stress hysteresis overall. Also, the initial (and final) elastic modulus is noticeably less than for the other two components. The 7×7 cable response (Experiment C1c) was analyzed in detail in Section 5.2 of Part I, so below we focus on the responses of the core wire and the 1×7 strand.

3.1. Core wire (7×7 cable)

The mechanical response of the core wire from the 7×7 cable in Fig. 2 exhibits the typical isothermal, outer-loop superelastic behavior with sharp transitions between elastic and transformation behavior and very flat load plateaus. Within the noise of the specimen thermocouple ($\approx \pm 0.1^\circ\text{C}$) and the sensitivity of the IR camera ($\approx \pm 0.1^\circ\text{C}$), no temperature changes were detected during the experiment. The force–elongation curve has an initial linear elastic segment during elastic straining of austenite, followed by a flat load (engineering stress) plateau ($A \rightarrow M^+$ transformation) during loading, and then an abrupt, but short, upturn after this plateau. Initial unloading has a nonlinear response with a positive but monotonically decreasing tangent modulus, which is interrupted by a $M^+ \rightarrow A$ localization event outside the LE gage length; thus the LE strain records a momentary increase in strain and the force rises to comply with global compatibility between the grips (see the inverted peak at the onset of the lower plateau). Further reverse $M^+ \rightarrow A$ transformation during unloading occurs along the lower load plateau, and once the lower load plateau is exhausted, the wire unloads along a steep linear elastic segment to zero load. All of these features have been shown and explained before in the tensile response of superelastic NiTi wires (Shaw and Kyriakides, 1995; Liu et al., 1998; Sun et al., 2000; Iadicola and Shaw, 2002; Chang et al., 2006), but a review is worthwhile to establish a baseline understanding for the more complex behavior of the other cable components discussed subsequently. Also, the DIC measurements here provide more quantitative data than in the past and a particularly clear view of the localized strain fields.

The axial DIC strain contours shown in Fig. 3 were generated in a similar manner as the IR temperature contour plots introduced in Part I. Axial strain profiles were extracted from DIC images at 40 s intervals, laid side-by-side (405 images) and synchronized with time (t) to obtain a contour map of the axial strain field history, $E_{zz}^L(z, t)$. The axial coordinate (z) has been normalized by the initial free length of the wire (L), and the vertical scale spans a limited field of view (FOV) from $z/L = 0.2$ to 0.4 , due to a limit on the resolution of the CCD cameras. The strain field is shown in the Eulerian frame (current configuration), so the bottom of the DIC analysis area moves up during loading and down during unloading as new material points appear in the FOV (for which we do not have their reference position). The axial stress history is overlaid for reference, and its scale is the right-hand vertical axis.

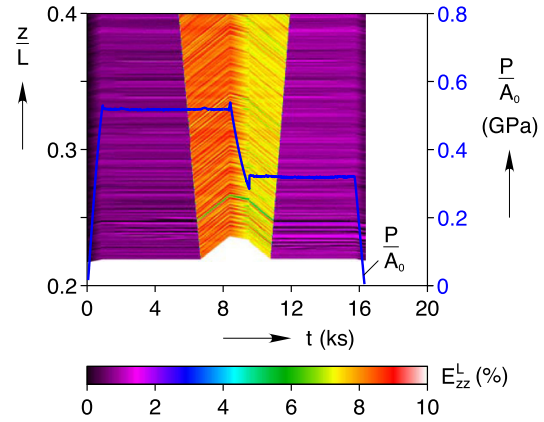


Fig. 3. Experiment W1b (straight core wire from the 7×7 cable at $\dot{\delta}/L = \pm 1 \times 10^{-5} \text{s}^{-1}$). Histories of axial stress (overlaid) and DIC axial strain field (contour plot) in a limited FOV. A single transformation front is visible as a near strain discontinuity, propagating at constant rate from the top to the bottom of the FOV during the loading force plateau, and propagating from the bottom to top during the unloading force plateau.

The sharp transition between high strain and low strain regions in Fig. 3 clearly shows a transformation front (a strain discontinuity) traversing the specimen length from top to bottom during the loading stress plateau ($A \rightarrow M^+$), and then from bottom to top during the unloading stress plateau ($M^+ \rightarrow A$). These strain discontinuities separate nearly homogeneous regions of low (A) and high (M^+) strain. The slight striations in the strain field allow one to observe the displacement of material points in time, and a clear kink in the displacement field is seen across each propagating front. Upon closer inspection, the DIC measurements show that the front is not actually a strain discontinuity, but instead a region of high strain gradient (macroscopic neck) with an axial extent of about $\Delta z^* = 0.27 \text{ mm}$ (about one wire diameter). This is expected considering that compatibility of radial displacements must be enforced between a given cross-section and its neighbor. The relevant length-scale for the neck is, therefore, the wire diameter.

Despite our limited FOV, we can deduce the number of fronts traversing the specimen from the speed of the fronts visible in Fig. 3. The speed of each front is nearly constant, measured as 0.0108 mm/s during $A \rightarrow M^+$ and 0.0121 mm/s during $M^+ \rightarrow A$. As derived in Shaw and Kyriakides (1995), the speed of front motion can be predicted for steady-state conditions as

$$c = \frac{\dot{\delta}}{n\Delta\varepsilon}, \quad (1)$$

where $\dot{\delta}$ is the prescribed elongation rate, n is the number of propagating fronts, and $\Delta\varepsilon$ is the strain jump across a front (idealized as a discontinuity). The equation is valid for isothermal transformation (constant strain jump) and all fronts moving at the same speed, which tends to be true to minimize temperature excursions. Note that the length of the wire specimen (L) does not appear in Eq. (1), so the front speed is independent of specimen length. If, however, we multiply and divide by L , then Eq. (1) becomes

$$c = \left(\frac{L}{n\Delta\varepsilon} \right) \frac{\dot{\delta}}{L}. \quad (2)$$

Thus, varying the specimen length, while holding the global strain rate ($\dot{\delta}/L$) fixed, will produce different front speeds. For a single moving front ($n = 1$), the predicted front speeds from this equation are $c = 0.0104 \text{ mm/s}$ during $A \rightarrow M^+$ and 0.0121 mm/s during $M^+ \rightarrow A$, where we used the strains at the onset and termination of the stress plateaus in Fig. 2 to find the respective strain jumps, $\Delta\varepsilon = 7.32\%$ and -6.28% . The predicted speeds agree well with the

measured ones, indicating that a single constant-speed $A \rightarrow M^+$ front traversed the entire specimen from top to bottom during loading, and then a single $M^+ \rightarrow A$ front traversed the entire specimen from bottom to top during unloading. Based on the observed front motion here and our experience from IR imaging in many other similar experiments, the $M^+ \rightarrow A$ nucleation event at the onset of the unloading stress plateau probably occurred quite close to the bottom grip, which momentarily created two diverging fronts, but the lowermost one immediately reached the grip leaving only a single upward moving front.

We can also use Eq. (2) and the measured axial extent of the front Δz^* to explain why NiTi wires are highly sensitive to the global strain rate $\dot{\delta}/L$. Solving Eq. (2) for $\Delta \epsilon$ and dividing by $\Delta t = \Delta z^*/c$, an estimate for the local strain rate as a front transits a given material point is,

$$\dot{\epsilon} \approx \frac{\Delta \epsilon}{\Delta t} = \left(\frac{L}{n \Delta z^*} \right) \dot{\delta} \quad (3)$$

Compared to the global strain rate ($\dot{\delta}/L$), the local strain rate ($\dot{\epsilon}$) is amplified by the factor in parentheses. For the case of a single moving front, $L/\Delta z^* = 282$ for our specimen, which is why even for thin wire, the experiment must be performed at an extremely slow global strain rate ($\dot{\delta}/L = 1 \times 10^{-5} \text{ s}^{-1}$) to achieve isothermal conditions in stagnant air. Aside from the important influence of the ambient medium, what constitutes a sufficiently slow rate clearly depends on the length of specimen. This is a common pitfall in our experience, counter to the usual expectations for material testing. One must be aware that when transformations occur via propagating fronts, longer SMA specimens are more rate-sensitive than shorter ones for the same global strain rate.

3.2. Core strand (7 × 7 cable)

The similarity of the 1 × 7 core strand’s mechanical response to that of its core wire can be attributed to the shallow helix angle

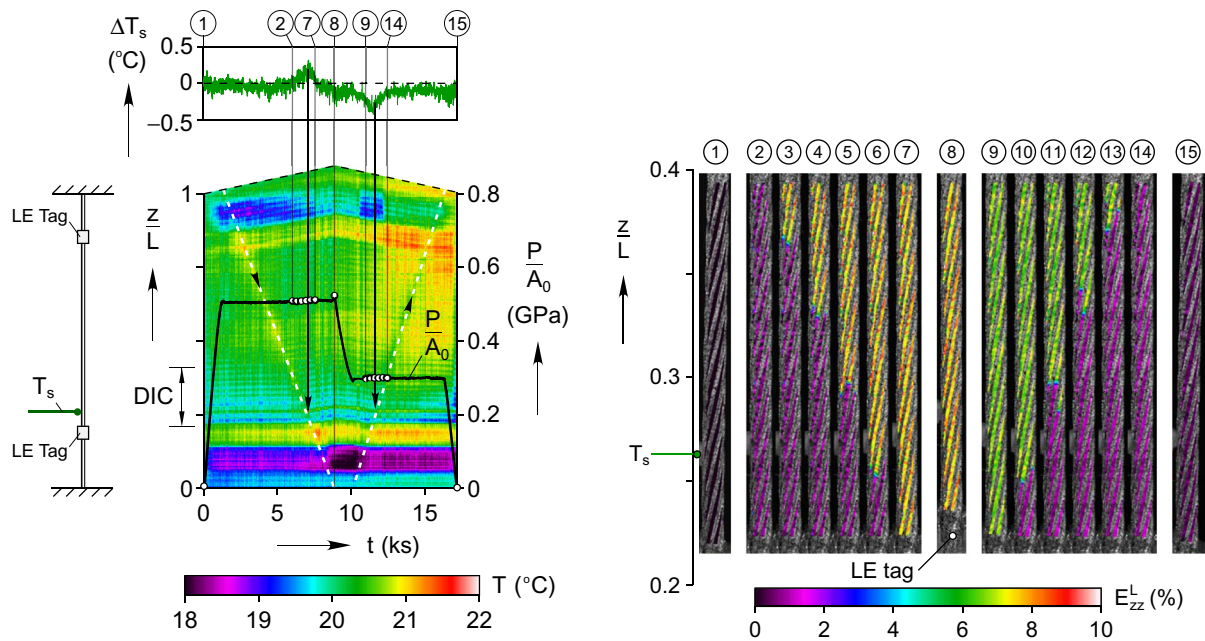
($\alpha_0^B = 11.3^\circ$) of the wires to the tensile axis, but quantitative differences exist. The end of the core strand plateau increases from $\delta_e/L_e = 8.04^\circ$ to 8.55° , at the cost of a small decrease in loading plateau stress from 517 MPa to 506 MPa. Assuming pure tensile loading in each wire at an $A \rightarrow M^+$ transformation stress of $\sigma^* = 517 \text{ MPa}$, a rough calculation to account for the six helical wires is

$$\begin{aligned} \frac{P^*}{A_0} &= \left(\frac{n^A \cos \alpha_0^A + n^B \cos \alpha_0^B}{n^A + n^B} \right) \sigma^* = \left(\frac{1 + 6 \cos 11.3^\circ}{7} \right) 517 \text{ MPa} \\ &= 508 \text{ MPa}, \end{aligned} \quad (4)$$

which agrees well with the measured value of 506 MPa. A small torque measured for the core strand was well under 1% of the torque cell capacity (2824 N-mm) and was not sufficiently accurate to generate a meaningful torque-response curve. Based on a similar calculation to Eq. (3), the estimated torque during transformation is

$$M_z^* = n^B r_0^B \sin \alpha_0^B \sigma^* \frac{\pi}{4} d^2 \approx 10 \text{ N-mm}. \quad (5)$$

The IR contour plot and specimen thermocouple history in Fig. 4(a) indicate that forward and reverse transformations each occur via a single global transformation front traversing the core strand gage length. (The location of specimen thermocouple and LE tags are shown on the scaled schematic of the specimens to the left of the IR contour plot.) The specimen thermocouple history (top plot of Fig. 4(a)), while somewhat noisy in this small temperature range, shows a small 0.25°C transient above ambient during the loading plateau between ⑤ and ⑥ and then a small -0.25°C transient below ambient during the unloading plateau near ⑩. In this case, the larger diameter of the core strand (3× the core wire) and the thermal scaling (increased volume/exterior surface area) allowed infrared imaging to be performed. The contour plot in Fig. 4(a) was generated in the same fashion as that of Fig. 3, except temperature is the field variable, and the entire gage length is visible. At this slow loading rate, the relevant temperature changes are small and can be masked by other artifacts. The core strand is only 1 pixel wide as



(a) Histories of IR temperature field (contour plot), stress (overlaid), and specimen thermocouple (above)

(b) Selected DIC axial strain field images

Fig. 4. Experiment S1a (1 × 7 core strand from the 7 × 7 cable at $\dot{\delta}/L = \pm 1 \times 10^{-5} \text{ s}^{-1}$). A single faint transformation front (highlighted by the dashed white line) can be seen in the IR contour plot (a), propagating at constant speed from the top to the bottom grip during loading ($A \rightarrow M^+$), and the reverse direction during unloading ($M^+ \rightarrow A$). Each global front is more clearly seen in the strain field images (b) as clustered, staggered fronts in individual wires.

viewed by the 256×256 IR sensor. The core strand was not perfectly aligned in the sensor, especially above and below the LE gage length, so the incident infrared radiation was split between two pixels in these areas and the temperature measurement was inaccurate at the specimen ends. In addition, during unloading the LE gage length is about 1°C warmer than during loading, due to a small temperature increase in our laboratory (T_a) over the five hour experiment. (Cleaner IR contour plots are obtained at higher rates, as in Fig. 13c of Part I and in Chapter 5 of Reedlunn (2011).) Nevertheless, close inspection does show a slight warm spot ($A \rightarrow M^+$ front) moving downward during the loading plateau, and then a slight cool spot ($M^+ \rightarrow A$ front) moving upward during the unloading plateau. Dashed white lines have been overlaid in Fig. 4(a) to highlight these locations, showing each front propagated at nearly constant speed, quite similar to the front kinetics during the core wire experiment. These fronts also coincide with the location and times the specimen thermocouple recorded the $\pm 0.25^\circ\text{C}$ transients (see the vertical arrows overlaid for reference).

The axial strain field images in Fig. 4(b) give a magnified view of the lower third of the laser extensometer gage length, and show that the macroscopic front consists of staggered fronts in the individual wires. The circled numbers above the DIC images in Fig. 4(b) correspond to the numbers above the specimen thermocouple history and the points overlaid on the stress history in Fig. 4(a). Consistent with the IR contour plot, the $A \rightarrow M^+$ front enters the DIC FOV between image ② and ③, and by image ⑦ has exited the FOV. The staggered fronts in the individual wires revolve around the tensile axis during the overall propagation of the macroscopic front. Close inspection of a video of the complete set of DIC images also shows that fronts in individual wires never pass each other as they propagate. For example, image ③ shows a staggered pattern of three fronts with the centermost front slightly ahead of the other two at $z/L = 0.37$. This centermost (wire) front appears again in the same wire in image ⑥ at $z/L = 0.25$, one pitch below (a single turn of its helix by counting down the strand by six wires) and the staggering is the same between fronts in adjacent wires. This staggering is similar to what was observed in the 7×7 cable in Part I, and the explanation is the same. Staggered fronts distribute the individual heat sources, thereby minimizing temperature deviations from ambient and any consequent axial stress changes. They remain clustered within about one strand diameter to minimize incompatibility within a given cross-section, which would be severe if one wire front greatly outpaced the others.

Although the core wire, core strand, and full cable have similar mechanical responses, slight differences in their thermal behavior at this slow strain rate of $\dot{\delta}/L = \pm 1 \times 10^{-5} \text{ s}^{-1}$ are harbingers of large differences in their mechanical response at higher strain rates. In the single core wire, the temperature excursions as the front passed by the specimen thermocouple were less than the inherent noise in the thermocouple used ($\pm 0.1^\circ\text{C}$). Yet the temperature excursions were about $\pm 0.25^\circ\text{C}$ for the core strand (see Fig. 4(a)) and $\pm 0.75^\circ\text{C}$ for the full cable (see Fig. 8 in Part I) for the same global elongation rate. This shows that enthalpy changes are dissipated less quickly in the larger diameter core strand and cable, but we expect probably not as slow as in monolithic rods of the same diameters.

4. Isothermal responses of the 1×27 cable components

Experimental responses of the four selected components of the 1×27 cable (core wire, 1×6 strand, 1×15 strand, and full cable) are presented below. Due to the decreased rate-sensitivity of the 1×27 components, these experiments were performed at $\dot{\delta}/L = \pm 1 \times 10^{-4} \text{ s}^{-1}$ which still produced nearly isothermal responses. Rather than pulling specimens to the end of a loading plateau, which often did not exist, an incremental loading

procedure was performed. This consisted of elongation-controlled cycles to progressively greater maximum strains, $\delta_e/L_e = \{7, 10, 20, 30, 40\}\%$, in all components, except the core wire which also included a cycle to 6.3% . Some experiments were halted when the specimen failed, and in others the test was stopped short of failure to disassemble and inspect the specimen. Below, Section 4.1 presents the measured responses, first providing an overview and then details of each experiment on the four selected components, progressing upward in the specimen hierarchy. Section 4.2 follows with a discussion of the deduced responses of the individual layers (see again Fig. 1(b)) obtained by subtracting pairs of measured responses.

4.1. Measured responses

Fig. 5 provides a quick overview of the mechanical responses of the four selected components, showing just the outer loading envelopes of the incremental cyclic responses detailed later in Figs. 6, 7, 9, and 10. As will be shown, the axial load and reaction torque returned to nearly the same global stress values upon reloading to the previous cycle's maximum δ_e/L_e . Consequently, the responses shown in Fig. 5, made of discrete loading segments of the actual measured cyclic responses, all exhibit nearly smooth outer envelopes, as if the loading took place without interruption.

Fig. 5(a) shows the progression in the force–elongation responses from the core wire to the full cable, where each component is successively more compliant (on a normalized basis) with the addition of each layer (B, C, D). Each layer has a deeper angle ($|\alpha_0|$) than the one underneath, and as with any standard coil spring, the normalized force is traded for greater elongation. Of course, the measured force is progressively larger for the larger components. For example, at $\delta_e/L_e = 10\%$ the force produced by the core wire, 1×6 , 1×15 , and 1×27 specimens are 54, 152, 264, and 399 N, respectively. Also, the force responses progress

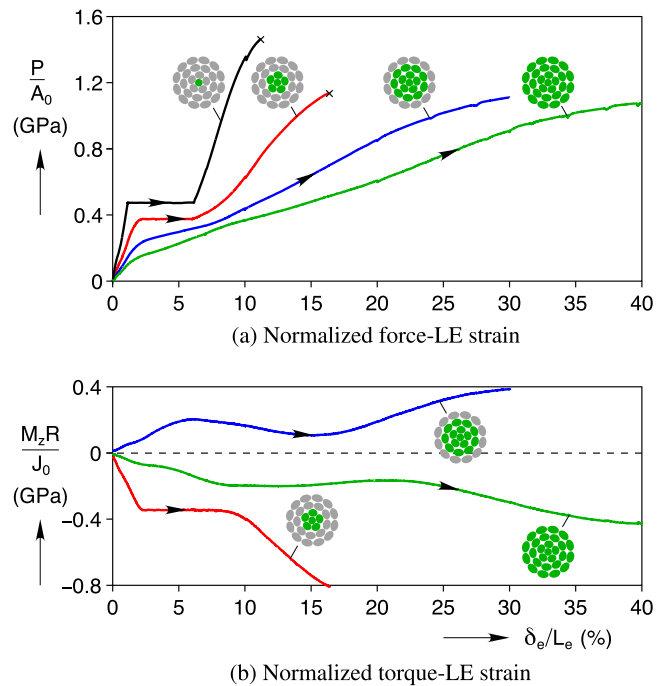


Fig. 5. Comparison of mechanical responses of 1×27 components (Exp. W2b, S2a, M2a, and C2d). Only the outer loading envelope of the incremental cycles of Figs. 6, 7, 9, and 10 are shown. The normalized force responses (a) show clear progression to larger overall compliance between successively larger components, yet the normalized axial torque responses (b) show more non-monotonic behaviors and less obvious trends from component to component.

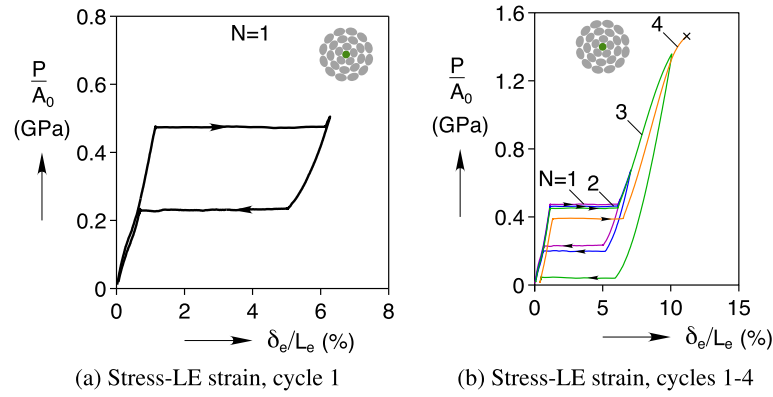


Fig. 6. Experiment W2b (core wire from the 1 × 27 cable at $\dot{\delta}/L = \pm 1 \times 10^{-4} \text{s}^{-1}$). Cyclic mechanical response taken to progressively larger load-unload cycles (specimen failure occurred during cycle 4 loading at $\delta_e/L_e = 11.2\%$).

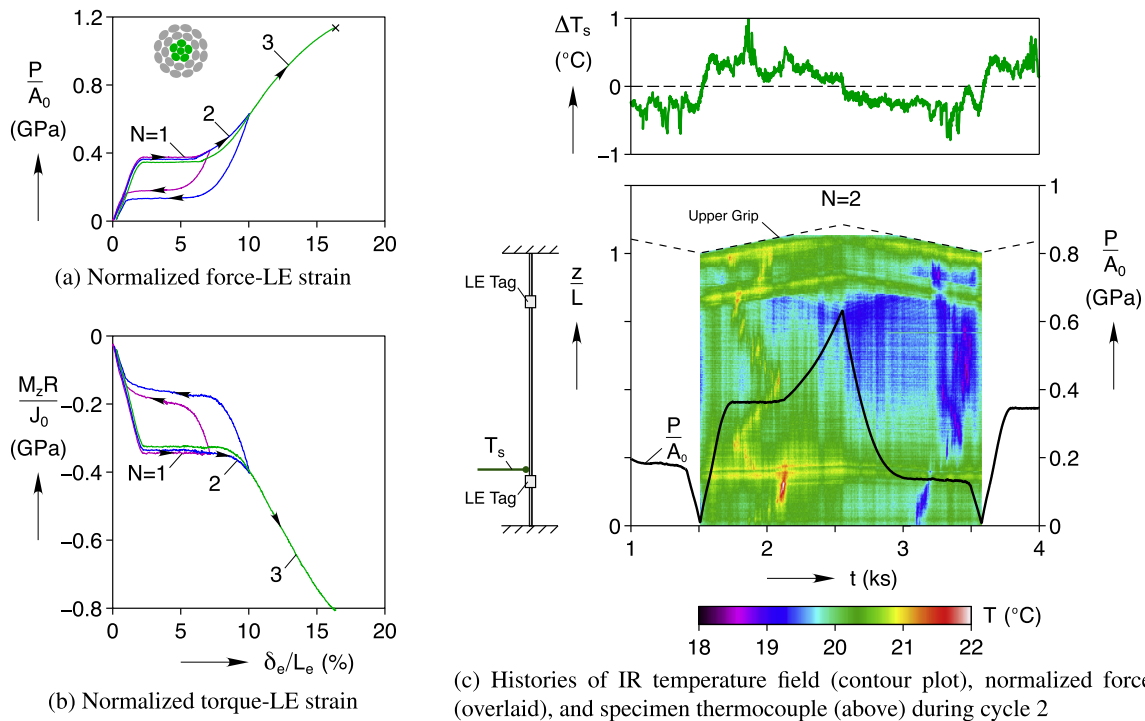


Fig. 7. Experiment S2a (1 × 6 core strand from the 1 × 27 cable subject to incremental cycles at $\dot{\delta}/L = \pm 1 \times 10^{-4} \text{s}^{-1}$). The normalized force response (a) is qualitatively similar to that of the core wire (Fig. 6) with force plateaus in the transformation strain range (2 to 6% strain), but quantitatively the 1 × 6 strand exhibits more compliant behavior and a larger ultimate failure strain at $\delta_e/L_e = 16.4\%$ (during cycle 3 loading). Interestingly, the normalized torque response (b) exhibits flat plateaus during loading in the transformation strain range, but not during unloading. The temperature blooms in the IR contour plot (c) appear to indicate propagating fronts in the specimen, but further inspection reveals these are instead isolated nucleation events that do not propagate.

from having clear load plateaus (core wire and 1 × 6 strand) to exhibiting nonlinearity but maintaining a positive tangent modulus (1 × 15 strand and 1 × 27 cable).

Fig. 5(b) shows a comparison of outer envelopes of the torque responses, progressing from negative to positive to negative values, moving up the hierarchy of components. According to our normalized torque metric, the 1 × 6 specimen has the largest relative torque of the three components, although again, on an absolute value basis the magnitude of the measured torque becomes progressively larger from the 1 × 6 strand to the 1 × 15 strand to the 1 × 27 cable. For example, at $\delta_e/L_e = 10\%$, the torques produced by the 1 × 6, the 1 × 15, and the 1 × 27 specimens are −13.9, 26.1, and −77.5 N-mm, respectively. The 1 × 6 strand has a relatively large, negative (due to the left-hand lay of layer B) torque reaction and is the only response with a flat moment plateau. Add-

ing layer C (right-hand lay) in the 1 × 15 strand causes the torque reaction to switch sign and to progress in an up-down-up manner with axial elongation. Adding layer D (left-hand lay) in the full 1 × 27 cable causes the torque to switch back to a negative sign and has a less dramatic up-down-up character. Each layer that is added has a deeper helix angle, more wires and a larger moment arm than the previous layer, so the outermost layer tends to dominate the torque response of the assembly. The alternating handedness also serves to keep the normalized torque relatively small in the full 1 × 27 cable, despite the large helix angles.

The progression in the mechanical responses in Fig. 5 suggests that the failure strain, or ductility, increases with each incrementally larger specimen. All failures observed here occurred at a grip, so these maximum strains should not be interpreted quantitatively as expected ductility values. Our grips were simple flat knurled

plates that clamped the specimens at their ends with significant radial pressure, so severe stress concentrations existed there. In engineering practice, structural cables are normally terminated by loops/crimps that are designed to minimize such stress concentrations. For the particular experiments in Fig. 5, the 0.226 mm core wire and 1×6 broke near the grips at the maximum strain shown, while the 1×15 and 1×27 did not break. In other experiments, however, the 1×15 and 1×27 broke at the grips within 1% strain of the maximum strains shown in Fig. 5. While these particular failure strains likely underpredict those that could be obtained with less severe end conditions, we believe the qualitative trends between the four components are representative, i.e., one can expect larger failure strains and enhanced compliance as more layers with large helix angles are added.

4.1.1. Core wire (1×27 cable)

The mechanical response of the core wire (experiment W2b, Fig. 6) exhibits distinct plateaus that persist even after loading to large strains. An enlarged view of cycle 1 is shown in Fig. 6(a), while all cycles (1 through 4) are shown in Fig. 6(b). The maximum strains of the first three load–unload cycles were $\delta_e/L_e = \{6.3, 7, 10\}\%$, respectively, and failure occurred during the loading portion of cycle 4 at a strain of 11.2%. The first cycle was strained to $\delta_e/L_e = 6.3\%$, just beyond the termination of the loading plateau, in order to capture the fundamental tensile response of the wire without introducing appreciable plasticity. The loading plateau during cycle 1 occurs at 475 MPa between $\delta_e/L_e = 1.1\%$ and 6.0% (plateau length of 4.9% strain), and the unloading plateau occurs at 231 MPa between $\delta_e/L_e = 5.0\%$ and 0.7%. The second cycle on the 1×27 core wire shows a small amount of shakedown, where the loading plateau is slightly lower (–12 MPa) than that of cycle 1. The unloading plateau during cycle 2 is lower than that of cycle 1 by a greater amount (–32 MPa) since unloading commenced from a maximum strain beyond the initial load plateau. Cycle 3 shows a further, but small, (–12 MPa) reduction in the loading plateau stress. Since Cycle 3 was strained well into the post-plateau regime, the unloading plateau is greatly lowered to only 42 MPa. Cycle 4 shows a more significant reduction in the loading plateau (by another –61 MPa). No unloading response for cycle 4 was measured, because the wire broke at the grips at $\delta_e/L_e = 11.2\%$ (1.46 GPa). DIC strain measurements (not shown here), exhibited a single propagating front during all load plateaus, quite similar to that shown in Fig. 3 for the 7×7 core wire. Note that the 1×27 cable is made of a different NiTi alloy than the 7×7 cable (as described in Part I), seen by the fact that the 1×27 core wire has slightly lower plateau stresses and significantly smaller plateau strains than the 7×7 core wire.

The small knee in cycle 1 at approximately $\delta_e/L_e = 0.5\%$ is due to a stress-induced transformation to the rhombohedral phase (R-phase) (Miyazaki and Otsuka, 1986), which has a small 0.2% transformation strain associated with $A \leftrightarrow R^+$ (as measured by the offset of two straight line fits on either side of the knee). When loaded at room temperature, this particular NiTi alloy undergoes a multistep transformation of $A \rightarrow R^+ \rightarrow M^+$. During unloading, this occurs in reverse, $M^+ \rightarrow R^+ \rightarrow A$. The longer, nearly flat, loading plateaus correspond to $R^+ \leftrightarrow M^+$ transformations, but the $A \leftrightarrow R^+$ transformations become more noticeable in the 1×6 , 1×15 , and 1×27 responses shown below because their effect is amplified by the helical wire geometries.

4.1.2. $1 \times$ Strand (1×27 Cable)

The cyclic force–elongation response of the 1×6 core strand (experiment S2a, Fig. 7(a)) is similar to that of the core wire (experiment W2b, Fig. 6), despite the substantial helix angle ($\alpha_B^0 = -30.4^\circ$) of the five outer wires (layer B). In fact, during cycle 1 (taken to 7% maximum strain) the load plateaus of both compo-

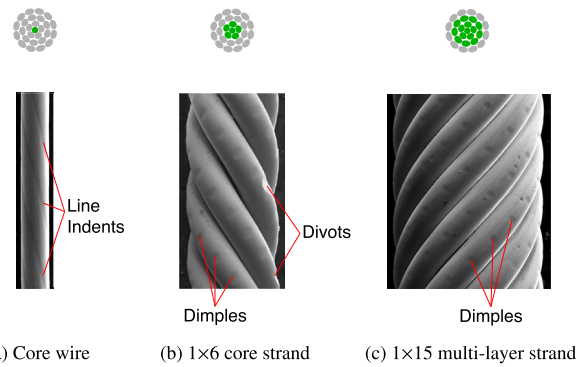


Fig. 8. Scanning electron microscope (SEM) images of 1×27 components, showing (likely pre-existing) Hertzian line indents, dimples, and a few divots resulting from contact of outer layers previously removed.

nents terminate at $\delta_e/L_e = 6.0\%$. The shakedown progression of the 1×6 core strand is also similar to that of the core wire. Each cycle causes small reductions in loading plateau stresses and larger reductions in unloading plateau stresses, since each cycle was taken to progressively larger maximum strains/stresses. A few differences do exist, however. The secant modulus (including the R-phase transformation) from 0% strain to the onset of the loading plateau knee ($\delta_e/L_e = 1.5\%$) is 21 GPa, approximately half of the corresponding secant modulus of the core wire (41 GPa, 0–1.1% strain). The onset of the 1×6 loading plateau is less sharp, occurring between $\delta_e/L_e = 1.5$ and 2.2%, and the plateau stress is lower ($P/A_0 = 374$ MPa, compared to 475 MPa in the core wire). The 1×6 strand failed (again at a grip) during cycle 3 loading at $\delta_e/L_e = 16.4\%$ (1.14 GPa, 275 N), which is 5.2% strain beyond the failure strain of the core wire.

The 1×6 torque response in Fig. 7(b) is nearly a mirror image of its force response. The character of the force and torque responses deviate slightly between $\delta_e/L_e = 6.0\%$ and 8.0%, where the axial load stiffens yet the torque remains relatively flat. The core wire is largely responsible for the axial load upturn as the strain exceeds its plateau strain, but the core wire has no contribution to the torque. By our simplistic metric the shear stresses in the 1×6 strand are substantial, yet the magnitude of the total torque is rather small, reaching a maximum of only 28.0 N–mm at the failure point.

The temperature field history of the 1×6 strand for cycle 2, taken to 10% maximum strain, is shown in Fig. 7(c). The temperature response exhibits small, isolated temperature rises/drops of about 1–2 °C from ambient ($T_a = 20.4$ °C) during the loading and unloading plateaus. The pattern of temperature deviations, especially during the loading plateau, suggests the existence of propagating transformation fronts along the specimen gage length, but this is not the case. The DIC strain fields (not shown¹) gave a magnified view of these regions and, although the local temperature deviations agreed spatially and temporally with localizations in the strain fields, the strain localizations did not propagate.

Upon subsequent investigation, the cause of localized strain and temperature was traced to preexisting geometric imperfections, as shown in the scanning electron microscope (SEM) images of Fig. 8. Although invisible to the naked eye, the micrographs show helical line indentations on the core wire and a periodic pattern of small dimples on the outer surface of the 1×6 and 1×15 strands. Each specimen was tested as shown, with the outer layer (s) removed, so

¹ Unfortunately, the DIC results for this particular experiment were lost in a computer hardware failure prior to publication, but similar strain fields in a 1×6 specimen can be found in Fig. 5.12 of Reedlunn (2011) at a higher loading rate ($\dot{\delta}/L = \pm 1 \times 10^{-3} \text{ s}^{-1}$).

while the SEM images in Fig. 8 were taken after mechanical testing, it is unlikely the surface indentations were caused by the experiments. Instead, the surface indentations most likely existed prior to the experiments, caused by the cable forming process. During manufacture, the alternating layers were tightly wound around each other, creating large contact stresses, and then shape set (heat treated near 500 °C for several minutes), which froze the indentations in place. In addition, the 1 × 6 has a few divots of missing material (Fig. 8(b)), creating even more severe stress concentration sites. The line indents likely had little effect on the core wire's response, but the dimples/divots in the 1 × 6 and 1 × 15 strands create noticeable strain field perturbations, as will be seen in the next section for the 1 × 15 strand.

To conclude the discussion of the 1 × 6 strand, it is interesting to compare its response with that of the 1 × 7 strand from the 7 × 7 construction. The two strands have similar constructions with the same normalized helix radius ($r_0^B/d = 1$) in layer B wires. However, the 1 × 6 has a helix angle of $\alpha_0^B = -30.4^\circ$, while the 1 × 7 strand has a helix angle of 11.3° . A direct comparison is not possible since the strands are made of wires of somewhat different NiTi alloys, but we can compare the relative changes in response from each core wire to its corresponding strand response. In the 1 × 7 strand, the loading plateau stress was 2.1% less than that of its core wire (Fig. 2). In the 1 × 6 strand, the loading plateau was 20.9% less than that of its core wire (375 MPa versus 474 MPa). While the simple calculation of Eq. (4) gave a reasonable prediction

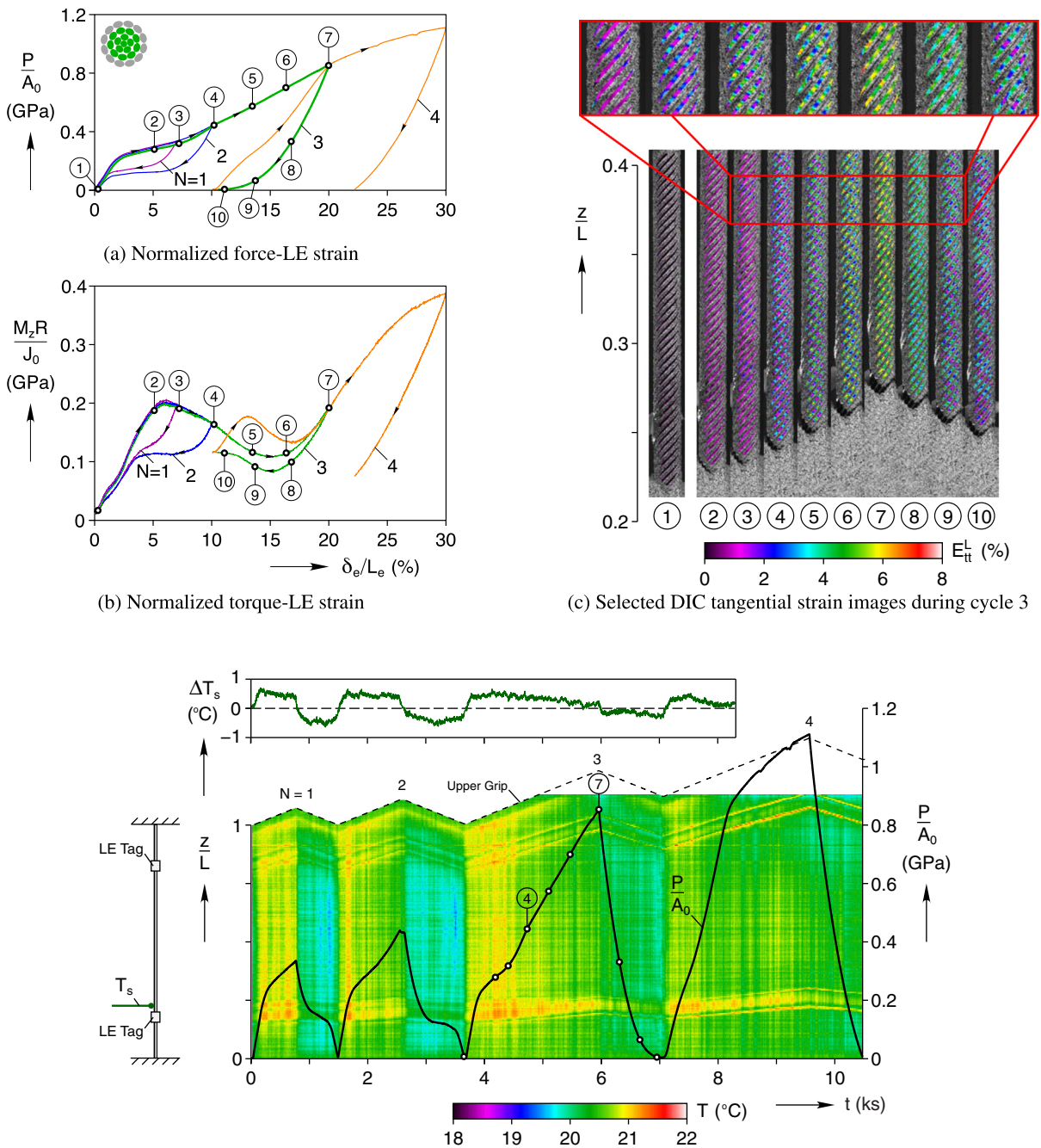


Fig. 9. Experiment M2a (1 × 15 strand from the 1 × 27 cable subjected to incremental cycles at $\dot{\delta}/L = \pm 1 \times 10^{-4} \text{s}^{-1}$).

of the loading plateau in the 1×7 strand, it overpredicts the transformation stress for the 1×6 strand, giving $475 \text{ MPa}(1 + 5 \cos -30.4^\circ)/6 = 421 \text{ MPa}$ versus the measured value of 375 MPa . This calculation ignores the effects of local wire bending and twisting on the axial transformation stress, so clearly these factors should not be neglected for these larger helix angles. Similar reductions in the axial transformation stress have been observed in tension–torsion testing of NiTi tubes (Sun and Li, 2002), so the multi-axial constitutive response is likely a similar contributor here, resulting in a suppressed resultant axial transformation force. Thus, a more complex analysis would be required to obtain a good quantitative prediction, which we leave for future work.

4.1.3. 1×15 Strand (1×27 cable)

The axial load response of the 1×15 multi-layer strand (experiment M2a, Fig. 9(a)) is quite different from the responses of the core wire and 1×6 strand. Here, the maximum strains for the four incremental cycles were $\delta_e/L_e = \{7, 10, 20, 30\}\%$. The large helix angle ($\alpha_0^c = 42.5^\circ$) and large helix radius ($r_0^c = 2d$) of the nine layer C wires have modified the behavior so that the axial load response bears little resemblance to the core wire response. Cycles 1 and 2 have a secant modulus of only 12.7 GPa at $\delta_e/L_e = 1.3\%$ in Fig. 9(a), tangent modulus changes are more gradual, and no force plateaus exist. Both of these cycles exhibit a superelastic loop and a small amount of shakedown. Cycles 3 and 4 are more extreme with maximum stresses of 853 MPa and 1.11 GPa , respectively, and have significant residual strains upon complete unloading (10.1% and 22.2% , respectively). The initial loading on the fourth cycle shows a sigmoid-like response with a gentle knee in the curve near 12% , which then stiffens until it meets the maximum load point of cycle 3. At this point the tangent modulus reduces to continue the prior loading curve where cycle 3 left off. Two small load drops occur at $\delta_e/L_e = 24.1\%$ and 27.4% during the remaining loading portion of cycle 4. Inspection of the specimen after the experiment confirmed that all wires remained intact, so the load drops were not due to any wire failures. The extensometer strain rate δ_e/L_e , however, did slow briefly during these load drops, indicating that the drops were due to grip slippage at these high loads. While this particular specimen did not fail after being subjected to 30% strain, other 1×15 specimens broke (at the grips) at similar strains, $\delta_e/L_e = 29.3\%$ and 26.8% , in two other experiments at higher elongation rates (see experiments M2b and M2c in Reedlunn (2011)).

The normalized axial torque response of the 1×15 specimen (Fig. 9(b)) is strikingly non-monotonic and path dependent. Cycles 1 and 2 exhibit wavy responses up to a local maximum at $\delta_e/L_e = 6.0\%$ (205 MPa on cycle 1), and upon unloading they both return to nearly zero torque. During loading in cycle 3, the torque undergoes a maximum near the same point as previous cycles, but then continues to drop until it reaches a local minimum of 108 MPa at $\delta_e/L_e = 15.1\%$ before increasing again to 191 MPa at the end of the loading segment. During unloading in cycle 3, the torque drops to another local minimum of 84 MPa (also near $\delta_e/L_e = 15\%$) and then rises to 117 MPa , at which point the axial load is zero. Cycle 4 has an up–down–up shape during loading that looks like a smaller, shifted, version of the cycle 3 loading response. Surprisingly, the loading path during cycle 4 rises above the previous cycle 3 response (at corresponding axial strains), reaching a local maximum of 177 MPa . The loading response during cycle 4 eventually rejoins the point at which cycle 3 left off at $\delta_e/L_e = 20\%$. Unloading during cycle 4 proceeds in a monotonic way similar to the axial load response, but a remnant torque still remains (75 MPa), although smaller than the remnant torque at the end of cycle 3 (117 MPa).

The intriguing torque response of the 1×15 strand is due to the alternating handedness of the layers. The torque response of the 1×15 specimen is dominated by the right-hand laid wires in layer

C and is therefore positive (Fig. 9(b)), unlike the negative torque response of the 1×6 specimen (Fig. 7(b)). Layer C has more wires than the left-hand laid wires in layer B (9 versus 5) and each layer C wire has twice the moment arm of a layer B wire. The oscillations in the torque response, however, are due to transformation activity occurring in the different layers at different LE strains δ_e/L_e . The alternating handedness of the 1×15 specimen has little effect on the axial load P , since $\cos(-\alpha_0) = \cos(\alpha_0)$ in Eq. (4), yet the handedness strongly affects the torque M_z , since $\sin(-\alpha_0) = -\sin(\alpha_0)$ in Eq. (5). Notice, for example, that the torque-rate changes sign during loading at $\delta_e/L_e = 6\%$, yet no corresponding change exists in the axial load response, except for the gentle upturn that occurs later at $\delta_e/L_e = 7\%$.

The torque response beyond $\delta_e/L_e = 10\%$ is difficult to interpret, since plasticity and phase transformation occur simultaneously. We can, however, make a few observations and venture plausible explanations.

- The axial load and torque both return to zero after cycles 1 and 2, but only the axial load returns to zero after cycles 3 and 4. This is likely due to uneven plastic deformation in the multi-layered construction of the 1×15 specimen. At zero load, the force carried in each layer may not be zero, only their sum. The total torque, however, would be zero only by chance at this point, since the layers contribute significantly different torques.
- We expect the outermost wires (layer C) to dominate the torque response of the 1×15 specimen. Thus, the layer C wires are likely responsible for the decrease in the torque seen between $\delta_e/L_e = 6\%$ and 15% during cycle 3. We hypothesize that once the axial strain reached about $\delta_e/L_e = 15\%$, the “easy” part of the transformation in the layer C wires was complete, and the local response in these wires stiffened to drive the overall torque back upward.
- By the end of loading in cycle 3, the layer B wires likely experienced significant plasticity. Without the ability to fully recover during unloading, layer B probably went into compression, generating a positive torque. This positive torque likely caused the upward shift in the 1×15 torque response during cycle 3 unloading and subsequent cycle 4 reloading.

Selected DIC strain images during cycle 3 are provided in Fig. 9c, and show a gradual, nearly uniform deformation during loading and unloading without propagating transformation fronts. Here, the tangential Lagrangian strain, E_{tt}^L , aligned with the centerlines of layer C wires, is shown instead of E_{zz}^L to give a better sense of the strain along the wires. The strain field (about ± 1 to 2%) in a checkerboard-like pattern (see the magnified view) due to the pre-existing dimples shown in Fig. 8(c). Constant strain contours occur at about -50° to the z -axis (see, for example, image ⑥), which is near $\alpha_0^D = -47.9^\circ$ (removed layer D wires). Comparing adjacent images, one can see that the strain field does not propagate, but instead the strain pattern generally intensifies/diminishes in magnitude. Other detailed observations of the DIC strain field (E_{tt}^L) sequence are as follows:

- ① The DIC strain field is nearly zero across the entire FOV at the onset of cycle 3 loading, despite the previous two mechanical cycles.
- ①–② The DIC strain magnitude grows uniformly. The axial load response has a knee at about $\delta_e/L_e = 2\%$ and the torque response is wavy between $\delta_e/L_e = 1$ and 2% .
- ②–③ The DIC strain reaches a nearly uniform magnitude of about 1% strain, but a few disparate striations of nominally 2% strain appear across the specimen, nearly perpendicular to the layer C wire axes (see the magnified view). The force shallowly rises, but the torque exhibits a local maximum.

- ③-⑤ A regular, periodic pattern of thin, high strain (about 5.5% in ⑤) striations develops over a background of 1% strain. The force rises at a somewhat larger rate, which remains relatively constant (nearly linear response) for the remainder of loading. The torque continues to drop.
- ⑤-⑥ The size and number of the striations remain relatively unchanged, but the DIC strain magnitudes increase, reaching 6% in the bands and 2% between the bands. The torque has a local minimum.
- ⑥-⑦ The high-strain striations remain static at about 6%, yet the strain between bands increases to about 5%. The strain field in ⑦ is more nearly uniform again. The torque increases rapidly.
- ⑦-⑧ The previously established strain pattern remains as the specimen unloads, but the strain levels diminish in a nearly self-similar manner to about 5% and 3.5% (respective high-strain/low-strain bands). The force and torque responses drop steeply.
- ⑧-⑨ The strain pattern begins to break up into an irregular pattern of striations (reaching about 3% and 1% in respective bands). The force response shallows to a lower (yet still positive) tangent modulus, but the torque response takes another upturn.
- ⑨-⑩ The high and low strain levels remain the same as before, but more striations partially or completely disappear. The force response continues to shallow to a nearly flat response at near zero load, but the torque continues upward (although reduced tangent modulus) to a residual value well above zero.

Certain features of the torque response can be correlated in time with the DIC strain field observations, but it is difficult to find any identifiable features in the axial load response that correlate to either the torque response or the DIC images. For example, the first inhomogeneities in the strain field appear between ② and ③, where the torque rate reaches a local maximum, yet no significant change exists in the axial load. Later, the torque rate changes sign again and reaches a local minimum between ⑤ and ⑥, yet the axial load response remains smooth and rather linear. In this case, however, the DIC strain field does not show any obvious changes in morphology, just an increase in strain magnitudes. During unloading, the torque reaches a local minimum between ⑧ and ⑨ when the DIC strain field transitions to a striated pattern, but the axial load response just continues to smoothly decrease its rate. Later, at ⑩ the torque response appears to be approaching another local maximum, yet the DIC strain striations still exist in a large portion of the specimen. While the high strain bands appear to be breaking up (the bands incompletely extend across the specimen width), we cannot claim this as a clearly defined morphology change to be identified with the local torque minimum. Any correlation at this point is vague at best, even with the torque response. Thus, DIC of the outermost wires gives useful information, but an incomplete view, of the entire specimen behavior. We will attempt to unravel the layer-by-layer mechanical response contributions in Section 4.2, and show a better a correlation with the DIC images shown here.

Table 3
LE strains and spatially-averaged DIC tangential surface strains (\bar{E}_{tt}^L) during experiment M2a on the 1×15 strand.

Cycle #	Max elongation		After unloading	
	δ_e/L_e (%)	\bar{E}_{tt}^L (%)	δ_e/L_e (%)	\bar{E}_{tt}^L (%)
1	7.0	1.0	0.1	0.0
2	10.0	2.1	0.2	0.0
3	20.0	5.2	11.1	2.3
4	30.0	8.0	22.2	5.3

Table 3 provides spatially-averaged axial (LE) and tangential strain (DIC) values at the maximum elongation and final unloading point ($P = 0$) for each cycle. It shows complete recovery of the average surface strains (\bar{E}_{tt}^L) in layer C wires at the end of cycles 1 and 2. The DIC strain field at the end of cycle 3 has an average residual strain of $E_{tt}^L = 2.3\%$, but we do not believe this is permanent deformation in layer C wires. At the onset of unloading ⑦ when the global strain is $\delta_e/L_e = 20.0\%$, the average tangential strain in layer C wires is $E_{tt}^L = 5.2\%$ and the maximum is only about 6%, which happens to correspond to the 6% strain at the termination of the loading plateau in the core wire response. Of course, the deformation in these wires is not purely uniaxial due to local twisting, but the tensorial shear strain is small, about 0.5% from DIC analysis not shown. The maximum strain reached in layer C wires appears to have remained within the transformation strain of M^+ . Accordingly, the remnant high strain striations in DIC image ⑩ appear to be the result of a structural effect, i.e., plastic (unrecovered) deformation in the inner layer wires causing antagonistic stresses between layers, rather than micro-structural damage in layer C wires themselves. The average strain recovery during cycle 3 unloading is $\Delta E_{tt}^L = 5.2 - 2.3 = 2.9\%$. Interestingly, average strain recovery during cycle 4 unloading is nearly as large, $\Delta E_{tt}^L = 8.0 - 5.3 = 2.7\%$, despite the prior strain of 8.0% at maximum elongation.

Finally, consistent with the strain field images, the temperature fields and thermocouple history in Fig. 9d show no evidence of propagating transformation fronts in the 1×15 strand. Overall, the specimen uniformly heats up by 0.5°C during loading and cools down by -0.5°C during unloading. A few experimental issues should be mentioned for completeness. First, the small stress relaxation at 2.55 ks during cycle 2 occurred while the load frame was being reprogrammed to return to zero load. Second, the ΔT_s data terminates at 8.3 ks because the thermocouple was detached from the specimen to avoid interfering with the LE tag that had translated upward at large strains. Third, the ambient temperature changed slightly between $t = 1.7$ ks and 2.3 ks during cycle 2. The drift in room temperature was removed from the thermocouple data by plotting the difference $\Delta T_s = T_s - T_a$, but it was not removed from the IR data. This explains why cycles 1 and 2 have a similar ΔT_s history, but the IR temperature field in cycle 2 appears to heat up only near the beginning of loading ($t = 1.6$ ks–1.7 ks). Fourth, the checkerboard strain field of Fig. 9c is not visible in the temperature field (Fig. 9d) since the strain inhomogeneities gradually appear and disappear, distributing the heat exchanges over time and space. Furthermore, the IR sensor did not have sufficient spatial resolution to pick up such fine features. In any event, the 1×15 specimen exhibits spatially uniform temperature fields similar to those seen previously in the full 1×27 cable (Fig. 14c in Part I), and the response here can be considered reasonably isothermal.

4.1.4. 1×27 Cable

The incremental cyclic response of the complete 1×27 cable, shown in Fig. 10, has many of the same features as the 1×15 specimen. The axial load response in Fig. 10(a) is similar in character, with nearly complete strain recovery during cycles 1 and 2 and a significant (although incomplete) 13% strain recovery during cycle 3. The addition of layer D wires to the 1×15 , however, reduced the axial load secant modulus from 12.7 GPa to 8.6 GPa (to the onset of the knee in the response at $\delta_e/L_e = 1.3\%$) and permitted a fifth cycle to $\delta_e/L_e = 40\%$. Although this specimen did not break on cycle 5, another 1×27 cable pulled at a higher strain rate (Exp. C2f in Reedlunn, 2011) did break near this maximum strain at $\delta_e/L_e = 39.2\%$. The seven small load drops during loading on cycle 4 and cycle 5 again all correlate with drops in the measured LE strain rate ($\dot{\delta}_e/L_e$), indicating the drops are due to grip slippage. Similar to

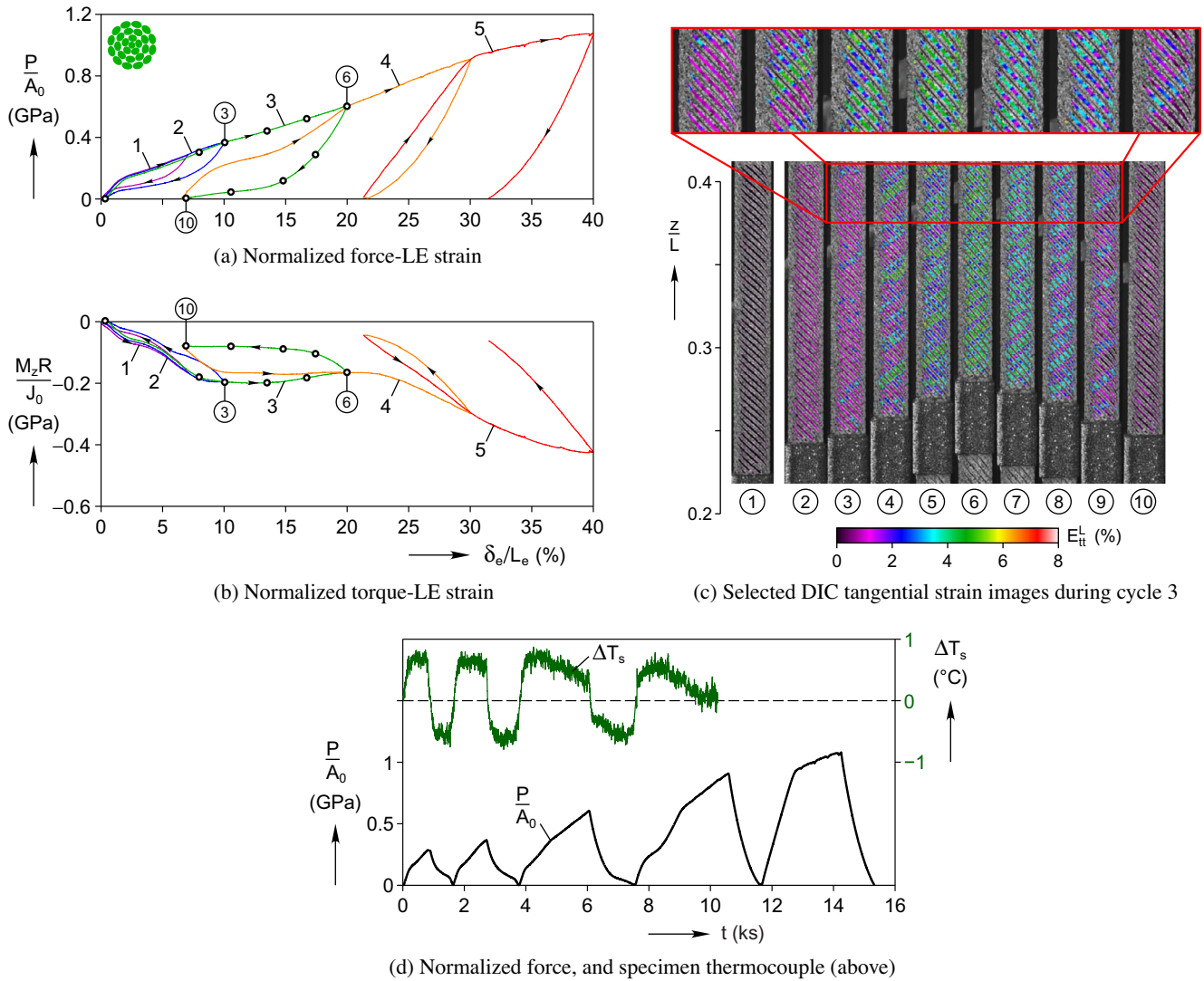


Fig. 10. Experiment C2d on 1×27 cable subjected to five incremental strain cycles at $\dot{\delta}/L = \pm 1 \times 10^{-4} \text{ s}^{-1}$.

the torque response of the 1×15 specimen, the torque response of the full cable in Fig. 10(b) is quite non-monotonic. The torque, however, switches sign again due to the addition of the 12, left-hand lay, layer D wires.

The DIC images of tangential strain during cycle 3 (Fig. 10(c)) exhibit uniform deformation until a few scattered strain localizations appear in image ③ at $\delta_e/L_e = 10\%$. Again, the appearance of localizations in the strain field between ② and ③ correlates with a decrease in the torque tangent modulus, but the load tangent modulus stays nearly constant. With further elongation, strain localizations develop in an irregular striped pattern until ⑥ ($\delta_e/L_e = 20\%$) when the surface strain field has filled into a nearly uniform value of about $\bar{E}_{tt}^L = 5\%$. Unlike the layer C wires, the outermost layer D wires of the full cable have no pre-existing dimples on their outer surface, so the strain field striations are less periodic. Along a given wire D in the magnified DIC images (④, for example), one can see pockets of transformed material (5% local tangential strain) of a few wire diameters in length adjacent to untransformed material (1% strain). The localized strain bands, however, still occur nearly perpendicular to the wires. In image ④ layer D's current helix angle is about -40° , while the strain band helix angle is about 50° . Upon unloading to zero axial force, ⑩, layer D wires have

Table 4

LE strains and spatially-averaged tangential surface strains (\bar{E}_{tt}^L) during experiment C2d on the 1×27 cable.

Cycle #	Max elongation		After unloading	
	δ_e/L_e (%)	\bar{E}_{tt}^L (%)	δ_e/L_e (%)	\bar{E}_{tt}^L (%)
1	7.0	0.5	0.2	0.0
2	10.0	1.2	0.5	0.0
3	20.0	3.9	6.9	0.4
4	30.0	6.2	21.7	3.8
5	40.0	9.1	31.5	6.0

recovered to about 0.4% local strain, despite the maximum elongation of this cycle ($\delta_e/L_e = 20\%$). For reference, Table 4 provides spatially-averaged axial (LE) and tangential strain (DIC) values at the maximum elongation and the end of each cycle.

The axial stress and specimen thermocouple histories for the full cable in Fig. 10(d) are qualitatively similar to the 1×15 response. An IR contour plot was created, but is not shown here, since it is quite similar to the 1×15 response and the one shown previously in Part I for the full cable. It confirmed uniform self-heating/self-cooling, consistent with the lack of temporal spikes

in the specimen thermocouple history. The specimen thermocouple transients are rounded step changes in temperature about ± 0.7 to 0.8 °C during the first three cycles, only slightly larger than in the 1×15 specimen. (The specimen thermocouple measurement ends near the end of cycle 4 loading since the thermocouple detached from the specimen.) Similar to Fig. 9d for the 1×15 specimen, the temperature excursions during cycles 3 and 4 taper off toward the end of loading, and temperature changes reaches zero during cycle 4 at $\delta_e/L_e = 24\%$ ($t = 9.5$ ks). This occurs at a few percent global strain after a nearly uniform strain field is reached (such as image ⑥ in cycle 3).

4.2. Deduced responses of individual layers

The aims of the remainder of this section, addressing 1×27 components, are to clarify the response of each layer of wires (B, C, and D), determine when transformations start and finish, and quantify their contributions to the total force and torque in the full cable. Since high-quality experiments on individual helical wires with constraint conditions representative of those in the full cable are extremely difficult to achieve, we instead deduced the response of each individual layer by subtracting of pairs of related components. For example, layer B's response was deduced by subtracting the core wire response from the 1×6 response at the same LE strains (δ_e/L_e). Note that the subtracted axial load responses from the 7×7 components were not shown in Section 3, because once normalized by the relevant cross sectional area, the subtracted responses were virtually identical to the corresponding component responses.

Clearly such a subtraction method should be used with caution, since the response of each outer layer is inferred, rather than directly measured, but the observations below support the validity of the following assumptions.

1. Cross-sections elongate and rotate as monolithic units.
2. Mechanical interactions between layers can be neglected.
3. Thermal interactions between layers can be neglected.

Assumption 1 appears to be valid, since we found no evidence of wires failing prior to the failure of the entire component and little evidence (if any) of relative sliding between wire layers. The responses in Fig. 5 are quite smooth, without any load drops large enough to indicate premature failure of a sub-layer or any single wire. We also disassembled unfailed specimens after mechanical testing to confirm all wires remained intact. These included the 1×15 specimen (Exp. M2a) and the 1×27 specimen (Exp. C2d). Since the 1×6 specimen failed during experiment S2a, an unbroken 1×6 specimen from another experiment (Exp. S2b in Reedlunn (2011)) taken to $\delta_e/L_e = 13\%$, still beyond the core wire failure strain in experiment W2b (11.2%), was disassembled and confirmed to have all wires still intact. Thus, it would appear that the outer layer of a given multi-wire component effectively shields the inner layers from the severe clamping stress at the grips, thereby allowing interior layers to be elongated further than when that layer was directly exposed to clamping during subcomponent testing.

The following steps were taken to confirm no significant relative sliding occurred in the interior layers of the specimens. Prior to the experiments, both ends of the specimens were cut to length using an abrasive cut-off wheel to create a flush end among all wires. After the experiment, but prior to disassembly, the ends were inspected under an optical microscope, and the wires were found to remain flush to within one wire diameter of one another. Furthermore, a specially prepared 305 mm long 1×15 specimen ($L = 269$ mm, and $L_e = 50.31$ mm) with welded ends was tensile tested to $\delta_e/L_e = 10\%$, and after testing the outer layers of the

strand were removed to confirm that the core wire was still attached to the welds. The mechanical response of this welded-end 1×15 specimen was confirmed to be the same as the outer envelope of cycles 1 and 2 in Fig. 9(a) and 9(b). Thus, we are confident that little or no relative sliding occurred in the inner layers during any of the experiments described above. Radial stresses between layers, caused by helical wires attempting to draw inward during elongation, were apparently large enough to prevent any significant relative sliding between adjacent layers in the cross-section. Even if local sliding did occur, when averaged over the 50 mm distance between the laser tags, the deviation in strain from layer to layer was likely minimal.

The validity of Assumption 2 is somewhat more arguable, but can be justified as follows, at least with respect to the global mechanical response. As a component is stretched, helical wires tend to radially contract, potentially causing large Hertzian contact stresses between adjacent wire layers. On the other hand, the contact areas were small compared to the distance between them along any given wire. Thus, although the contact may affect the local stress state, we expect the effect of mechanical interactions between layers to be small on average.

Assumption 3 is based from the fact that the elongation-rates were slow and the temperature transients were small for this set of experiments. The temperature of even the complete 1×27 cable only deviated from ambient air temperature by less than ± 1 °C. We additionally expect radial temperature gradients in individual wires and between adjacent layers can be neglected. Treating the cable as a monolithic element, the Biot number is low $Bi = hD/k_M = 0.017 \ll 1$, where $h = 90$ W m⁻² K⁻¹ is a conservatively high convective film coefficient for stagnant air, $D = 1.582$ mm is the specimen diameter, and $k_M = 8.6$ W m⁻¹ K⁻¹ is the conductivity of martensite (lower than austenite). This calculation ignores the fact that conduction is limited to the contact

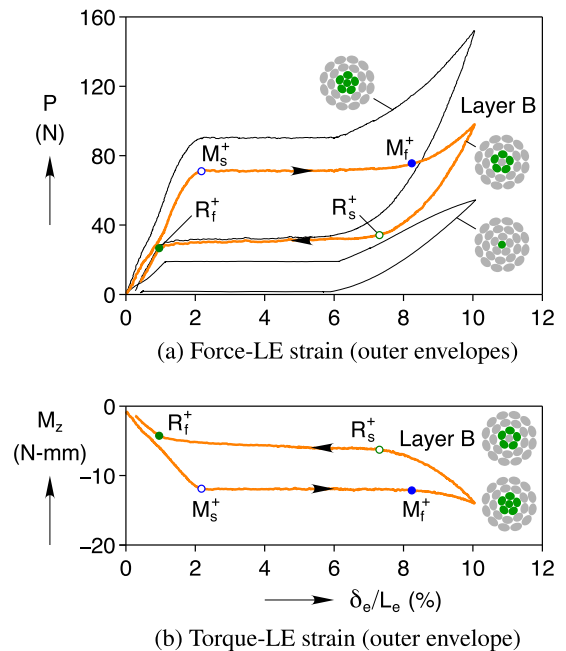


Fig. 11. Deduced response of Layer B wires (1×27 cable). Measured (un-normalized) axial load (a) and torque (b) responses of the core wire (outer envelope of cycles 1 through 3 from Exp. W2b) and the 1×6 strand (outer envelope of cycles 1 and 2 from Exp. S2a) are shown by thin lines, which were then subtracted to produce the deduced response of layer B (bold lines). The apparent force and torque responses of layer B now mirror one another, and characteristic features, such as the onset/termination of plateaus (points indicated), are well aligned with LE strain.

patches between the wires, but even a ten-fold decrease in effective k_M still results in $Bi \ll 1$.

4.2.1. Layer B

We first consider the innermost two components of the 1×27 cable. The deduced global mechanical response of layer B wires was obtained by subtracting the response of the core wire (layer A, Exp. W2b) from that of the 1×6 strand (layers A + B, Exp. S2a) as shown in Fig. 11. To keep the figure legible, only the outer envelopes of the loading and unloading responses are shown by piecing together relevant segments of responses of Figs. 6 (core wire, cycles 1 through 3) and 7 (1×6 strand, cycles 1 and 2). These estimate the isothermal responses that would be measured if the specimens were simply elongated to $\delta_e/L_e = 10\%$ and back to zero load without interruption. The measured axial force responses are shown in Fig. 11(a) by thin lines, and the deduced response for layer B by subtraction is shown by the bold line. The torque response in Fig. 11(b) is the measured response for the 1×6 strand, which is identical to the deduced response of layer B since the straight core wire has no torque contribution. Note that the axial load and torque responses are shown as raw measured force values (un-normalized) to clearly illustrate the subtraction process.

Fig. 11 reveals why certain features in the axial force and torque responses of the 1×6 strand do not line up, such as the lengths and termination points of the axial load and torque plateaus. In particular, the 1×6 axial load (Fig. 11(a)) suddenly increases at $\delta_e/L_e = 6.0\%$ (termination of the loading plateau), but the torque

(Fig. 11(b)) remains smooth and does not stiffen until beyond $\delta_e/L_e = 8\%$. Here, we see the core wire is solely responsible for the kink in the 1×6 strand force response, since the subtraction removed any such kink from the force response layer B. The apparent force plateau in layer B continues smoothly until about $\delta_e/L_e = 8\%$ before the response takes a gentle upturn, all of which are now mirrored in the torque response at the same elongation values. Presumably, the “easy” portion of $R^+ \rightarrow M^+$ transformation in the helical wires of layer B starts at $\delta_e/L_e = 2.2\%$ and does not complete until about 8 to 9% strain. Similar characteristic strain values can be identified for the $M^+ \rightarrow R^+$ transformation during unloading, since the force and torque plateaus (and other features) in layer B are now well correlated. Thus, we expect the deduced force and torque responses of layer B to reasonably capture the mechanical response of six helical springs stretched in parallel while constrained by an inner mandrel.

4.2.2. Layer C

The deduced response of layer C is obtained by subtracting the 1×6 response (Exp. S2a) from the 1×15 response (Exp. M2a), and is shown in Fig. 12. As before for clarity, only the outer envelope of cycle 1 and 2 are shown for the un-normalized force and torque responses (Figs. 12(a) and 12(b)). Figs. 12(c) and 12(d), however, show the normalized force and torque responses of layer C response during cycles 1 and cycle 2 and the loading portion of cycle 3. These were normalized by the reference area and torsion constant of layer C alone. The 1×6 strand failed during cycle 3, so

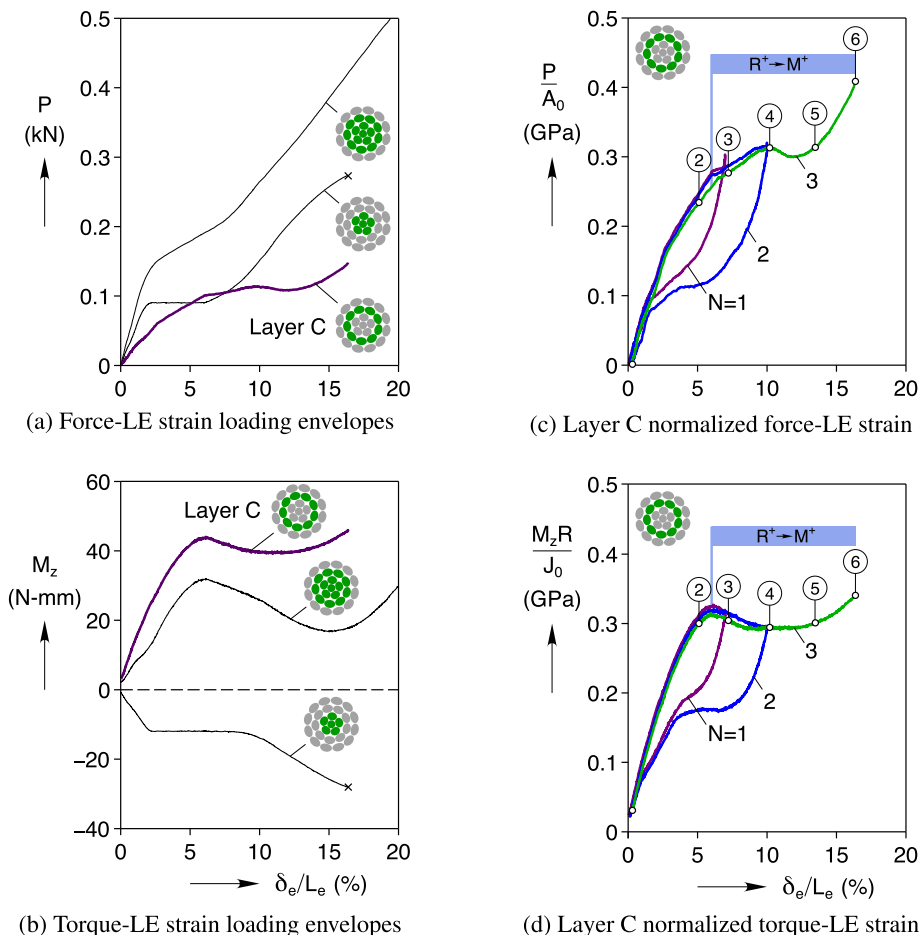


Fig. 12. Deduced response of layer C (1×27 cable). (a), (b) Measured axial load and torque responses (thin lines) of the 1×6 strand (Exp. S2a) and the 1×15 strand (Exp. M2a) and subtracted responses of layer C (bold line). Only the loading portion of cycles 1 through 3 are shown. (c), (d) Normalized axial load and torque responses of layer C for cycles 1 through 3. Circled labels correspond to DIC strain field images in Fig. 9c during cycle 3.

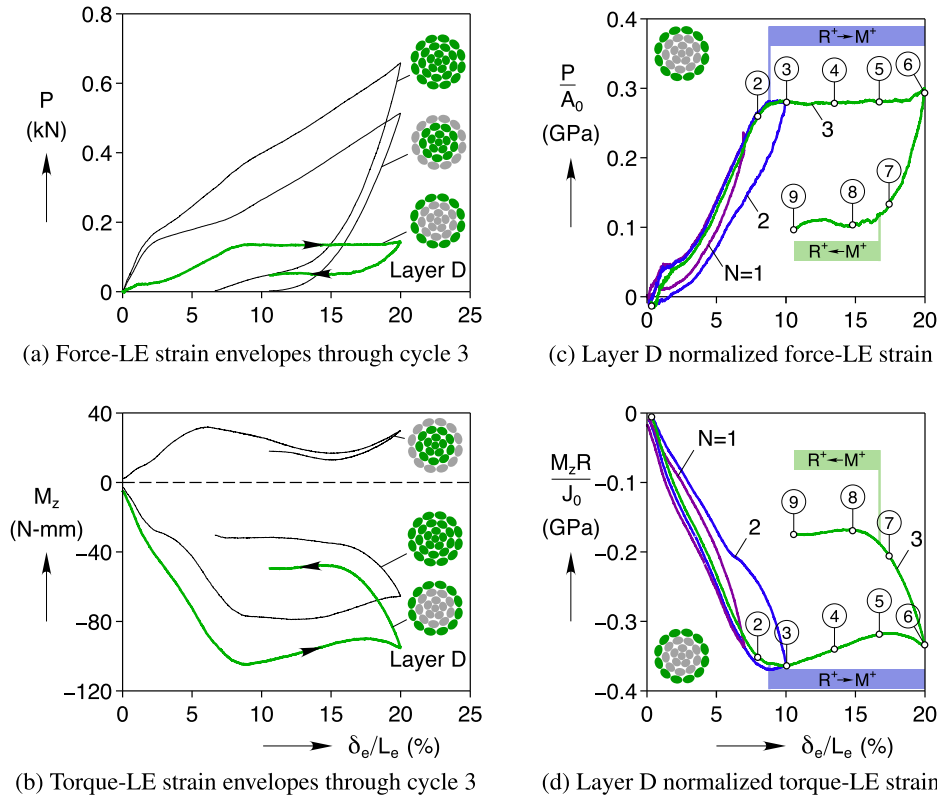


Fig. 13. Deduced response of layer D (1×27 cable). (a), (b) Measured axial load and torque responses (thin lines) of the 1×15 strand (Exp. M2a) and the 1×27 cable (Exp. C2d) and subtracted responses of layer D (bold line). Only the outer envelopes of cycles 1 through 3 are shown. (c), (d) Normalized axial load and torque responses of layer D for cycles 1 through 3. Circled labels correspond to DIC strain field images in Fig. 10(c) during cycle 3.

no subtraction was possible for unloading. The circled labels in Figs. 12(c) and 12(d) correspond to the strain field images of the 1×15 (Exp. M2a) in Fig. 9c during cycle 3 loading.

Several confusing aspects of the previous 1×15 results are resolved by the response subtraction.

1. During initial loading (below $\delta_e/L_e = 6\%$), the 1×15 torque (Fig. 12(b)) was slightly wavy with a knee in the torque at about $\delta_e/L_e = 1\%$, yet the DIC strain fields were relatively uniform (between ① and ② in Fig. 9c). After subtraction, the inferred torque of layer C is much smoother, with a monotonically decreasing tangent modulus up to the local torque maximum at $\delta_e/L_e = 6.0\%$.
2. The 1×15 torque had a local maximum at $\delta_e/L_e = 6.0\%$ where strain localizations began to appear between ② and ③, yet the axial load tangent modulus was relatively constant across this point. After subtraction, layer C's axial force and torque tangent moduli both change together at $\delta_e/L_e = 6.0\%$ in Figs. 12(a) and 12(b). What made this particularly confusing before was that the termination of the force plateau in the core wire occurred at $\delta_e/L_e = 6.0\%$, coincidentally the same point as the onset of $R^+ \rightarrow M^+$ transformation in layer C (see again Fig. 9c).
3. The 1×15 axial load exhibited a relatively constant slope between $\delta_e/L_e = 8$ and 20% , yet the torque had a local minimum near $\delta_e/L_e = 15\%$. After subtraction, layer C's axial load and torque both stiffen together. As one expects, the mechanical stiffening now coincides with the disappearance of low strain regions in Fig. 9c (⑤ through ⑦). Furthermore, the 1×15 torque (Fig. 12(b)) had a relatively constant negative slope between $\delta_e/L_e = 6$ and 11% , but thereafter drops more steeply (at least initially) due to the stiffening in the 1×6 negative torque's contribution. After subtraction, this kink in the torque response at 11% is removed in layer C's torque response.

Incidentally, a small spike appears during cycle 1 in the normalized axial load (Fig. 12(c)) just after the maximum value of δ_e/L_e . This spike is an artifact of subtracting two response curves that did not have the exact same maximum strain. The 1×15 specimen was stretched to $\delta_e/L_e = 6.98\%$, but the 1×6 specimen was stretched slightly further to $\delta_e/L_e = 7.12\%$, so the subtraction is inaccurate between these strains.

A few other details, however, are a bit perplexing. First, layer C's force response (Fig. 12(a)) is slightly wavy between $\delta_e/L_e = 1$ and 3% , which we presume is due to the $A \rightarrow R^+$ transformation, but layer C's torque response (Fig. 12(b)) is smooth in this range. We expected to see some "signature" of $A \rightarrow R^+$ transformation in the torque response. Second, the force "plateau" is somewhat wavy in layer C's response in Figs. 12(a) and 12(c) between $\delta_e/L_e = 6.0$ and 15% , and the extra bump near $\delta_e/L_e = 10\%$ is difficult to explain. This strain appears to correspond to stiffening in the 1×6 torque response and the local minimum in layer C's torque response. The DIC strain fields at ④ in layer C are striated (mid $R^+ \rightarrow M^+$ transformation) and do not saturate until much later. We expect that local strains in layer B saturate near $\delta_e/L_e = 10\%$ (although DIC is not available to confirm this), but it remains unclear why this would result in a softening in layer C's load response.

We speculate that this last difficulty could be related to the behavior of the core wire and Assumption 2 no longer being valid. The core wire is subjected to (lateral) radial pressure of varying degree from the outer wires in the 1×6 , 1×15 , and 1×27 specimens as they tend to draw inward during elongation. Although the lateral pressures are unknown, one can imagine it is small in the 1×6 specimen (from the five layer B wires), but much larger in the 1×15 specimen (from the 14 layer B and C wires). The experimental study of Jacobus et al. (1996) compared the responses of NiTi bars under tension and combined tension-lateral

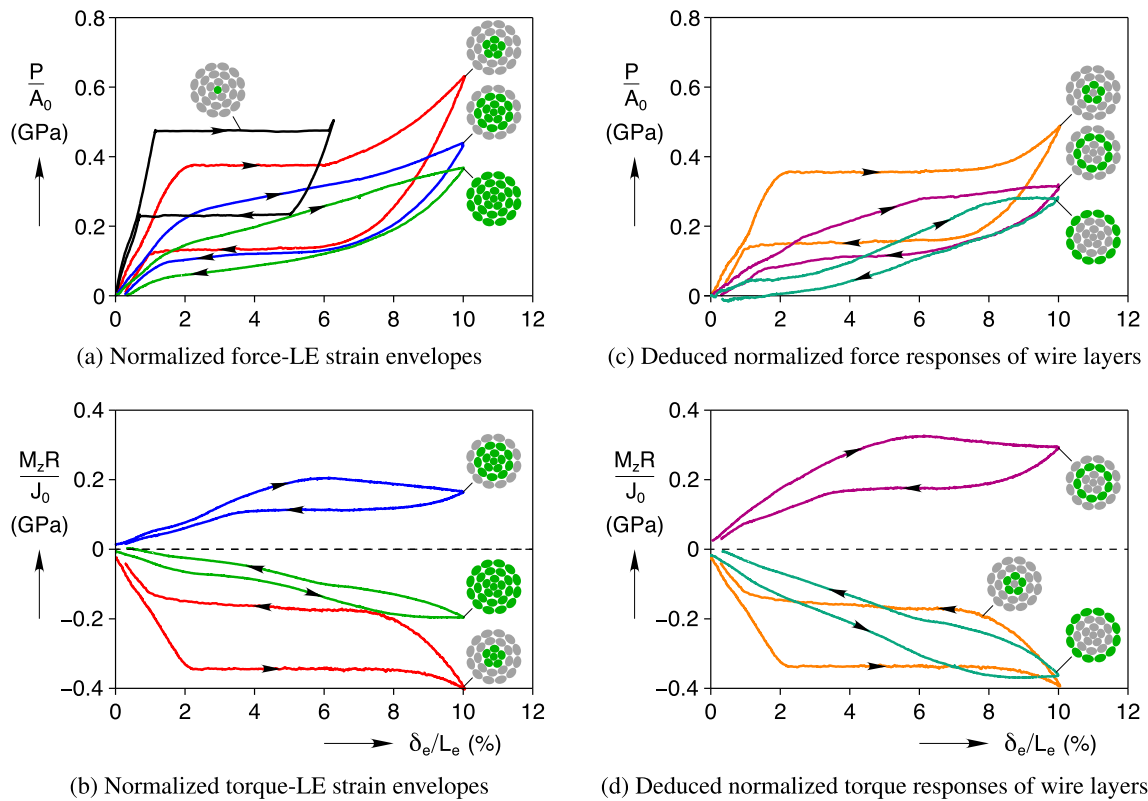


Fig. 14. Normalized mechanical responses of all 1×27 components and layers. (a) Measured normalized axial load responses of the four components tested: core wire (Exp. W2b, cycle 1), and cycle 1 and 2 outer envelopes of the 1×6 strand (Exp. S2a), 1×15 strand (Exp. M2a), and full 1×27 cable (Exp. C2d). (b) Corresponding normalized torque responses of the four components tested. (c) Deduced (subtracted), normalized axial load responses of the helical wire layers B, C, and D. (d) Corresponding (subtracted) normalized axial torque responses of layers B, C, and D.

pressure. In pure uniaxial tension, they measured the usual loading plateau in pure uniaxial tension, starting at 0.7% strain and ending (distinctly) at 6% strain; however, when a lateral compressive stress (equal to half the magnitude of the axial tensile stress) was applied, the axial load tangent modulus remained positive and constant from 0.7% strain to 11.5% strain (where they stopped collecting data). Accordingly, the effective core wire load response could have been different in the 1×6 and 1×15 specimens, and the response subtraction may not accurately reflect layer C's load response alone. Of course, if this is true, changes in core wire response have no adverse effect on the torque subtraction, which supports the fact that we observe the anomaly only in the subtracted force response. Furthermore, as will be shown below, layer D's force response has no such anomaly when the 1×15 response is subtracted from the 1×27 response. The 1×27 probably also applied a significant lateral compression to its core wire, but it may be similar inside the 1×15 specimen, if one accepts that adding additional layers will eventually produce a diminishing increase in the lateral pressure on the core wire. If the core wire responded the same in both specimens, then subtracting the 1×15 from the 1×27 effectively removes the effect of the core wire.

4.2.3. Layer D

The deduced response of the outermost layer D, shown in Fig. 13, was obtained by subtracting the response of the 1×15 strand from the response of the full 1×27 cable. Again, the thin lines in Figs. 13(a) and 13(b) are the measured outer envelopes (cycles 1 to 3) of the raw force and torque responses, respectively, while the bold lines are the subtracted response of layer D. Normalized force and torque responses for layer D, showing loading

and unloading cycles 1 through 3, are provided in Figs. 13(c) and 13(d). Note that during cycle 3 unloading, the subtracted response of layer D is incomplete because the 1×15 strand reached zero load at $\delta_e/L_e = 10.5\%$, at which point the 1×27 cable still carried 48 N of load.

The subtracted load response of layer D is remarkably clean with nearly flat plateaus in Fig. 13(a) during both $R^+ \rightarrow M^+$ (loading) and $M^+ \rightarrow R^+$ (unloading) transformations. The onset of the load plateau at $\delta_e/L_e = 8.8\%$ coincides with a decrease in the torque tangent modulus (see Figs. 13(c) and 13(d)) and the evolution from a uniform strain field in DIC image ② to a heterogeneous strain field in ③ (Fig. 10(c)). Subsequently, the negative torque in layer D first decreases in magnitude along a nearly linear path between ③ and ⑤, until about $\delta_e/L_e = 19\%$ when both the torque and the axial load gradually stiffen again. This stiffening coincides with a transition from a heterogeneous strain field in DIC image ⑤ to a more uniform field in image ⑥. Reverse transformation occurs during unloading along an approximate force plateau between $\delta_e/L_e = 16.7$ and 10.5% . Between ⑥ and ⑦, the stripes of low strain broaden a bit in Fig. 10(c), but whole stripes of high strain only start to disappear at the onset of the unloading plateau, from ⑦ to ⑧. By image ⑨ most of the high strain stripes have dispersed, and by image ⑩ (-3.7% strain below the last layer D data point) the strain field is uniform.

Additionally, a distinct knee exists in the initial loading response near $\delta_e/L_e = 2\%$, which is due to the small, but now more apparent, $A \rightarrow R^+$ transformation. Its transformation strain was about 0.2% in the core wire, but its effect is amplified nearly tenfold here to about 1.9% (as measured by the horizontal offset between pre- and post-knee tangent construction lines). In layer D, the $A \rightarrow R^+$ transformation is most apparent in the force response,

but upon close inspection a slight knee can also be discerned in layer D's torque response. It is interesting that the $A \rightarrow R^+$ transformation gives a more dramatic change in the force response compared to the torque response, while the $R^+ \rightarrow M^+$ produces a more dramatic change in the torque response (change in sign of its rate) compared to the force response (that simply reaches a plateau).

4.3. Comparison of 1×27 components and layers

Finally, a comparison of the normalized mechanical responses of the four 1×27 components and the three helical layers are summarized in Fig. 14. Measured force and torque response (normalized) are shown in Figs. 14(a) and 14(b), respectively. Deduced (subtracted) force and torque normalized responses of helical wire layers A, B, and C are shown respectively in Figs. 14(c) and 14(d). Except for the core wire response, which shows only cycle 1, all other components and layer responses are outer envelopes of cycles 1 and 2. Fig. 14(a) shows the clear progression to more compliant behavior in the normalized force responses from the core wire, 1×6 strand, 1×15 strand, to the full 1×27 cable. Although the torque responses alternate sign, the magnitude of the normalized torque responses follow the same progression. On a normalized basis, the 1×6 strand exhibits the greatest torque magnitude, and the full cable exhibits the least.

Similar to Fig. 14(a), the deduced (normalized) force responses of the helical layers in Fig. 14(c) show a progression from layer B to layer D to more compliant behavior, as is expected. However, the onset of transformations are more clearly defined and force plateaus are more evident as wires transform to M^+ . During loading, layer B exhibits a force plateau (despite the lack of any propagating fronts), while layers C and D exhibit approximate plateaus that have a slightly positive tangent moduli. The corresponding progression in normalized torque responses in Fig. 14(d) is similar to that of the tested components, where the axial torque alternates sign due to the change in handedness from layer to layer. The normalized torque magnitudes, however, are generally larger than their counterparts in Fig. 14(b) that included the interior layers. During loading, layer B exhibits a torque plateau, while layers C and D exhibit decreasing torque magnitudes during transformation to M^+ . More importantly, changes in force and torque in each layer (Figs. 14(c) and 14(d)) occur at the same LE strain, contrary to the force/torque responses of the tested components. To summarize, the onsets of $R^+ \rightarrow M^+$ transformation occur at $\delta_e/L_e = 2.2, 6.0, 8.8\%$, respectively, for layers B, C, and D. The corresponding terminations of load/torque plateaus occur at about $\delta_e/L_e = 8, 14, 19\%$ (referring back to Figs. 12 and 13 for layers C and D at large strains).

Before concluding, we should comment on the utility of subtracting the mechanical responses of components to infer the response of wire layers. Clearly, it is not a substitute for direct measurement. Even if our assumptions are perfectly satisfied, subtracting experimental data always magnifies errors. On the other hand, we found it useful to illuminate important features in the behavior without a large experimental effort. For example, in our early full 1×27 experiments (see Fig. 6a and Fig. 14 in Part I) we performed IR imaging without DIC. During loading, the axial stress tangent modulus changed at $\delta_e/L_e = 1.2\%$, but remained relatively constant beyond that. Similarly, the IR images showed a spatially uniform temperature field, which remained temporally constant beyond $\delta_e/L_e = 1.2\%$ (see Fig. 14c in Part I). Between $\delta_e/L_e = 1.2\%$ and 12% , it was quite difficult to determine when individual layers transformed. After performing experiments on the hierarchy of components of the 1×27 cable and subtracting the mechanical responses, the initial knee in the full cable's response at $\delta_e/L_e = 1.2\%$ was determined to be due

to $A \rightarrow R^+$ transformation. Furthermore, the start of $R^+ \rightarrow M^+$ transformation was identified by changes in tangent moduli of deduced layer B, C, D responses ($\delta_e/L_e = 2.2, 6.0, 8.8\%$, respectively). The DIC derived strain fields confirmed that transformation indeed initiated at these values of δ_e/L_e , but an engineer wishing to quickly assess a cable design can avoid the trouble of DIC measurements by simply subtracting the responses of its components.

5. Summary & conclusions

In Part I of this two part series, two shape memory alloy cable designs, a $7 \times 7 \times 0.275$ mm and $1 \times 27 \times 0.226$ mm construction, were introduced. Here in Part II, the cables were disassembled to examine the superelastic behavior of their sub-components at nearly isothermal loading rates. The significant conclusions are as follows:

1. The 1×7 core stand and full 7×7 cable had similar isothermal mechanical responses to that of the straight core wire. This similarity is largely due to the small helix angles in the design, which causes the wires to be loaded predominately in tension. As such, all three components exhibited propagating transformation fronts. Certain detailed observations were new, however, such as the staggered wire fronts in the 1×7 strand.
2. SMA cables are highly tailorable by their design, as illustrated by the wide range of mechanical responses from each of the 1×27 components. For example, the tensile secant modulus at $\delta_e/L_e = 2\%$ strain was 23.7, 18.4, 11.1, and 7.3 GPa for the core wire, 1×6 , 1×15 , and 1×27 cable, respectively, while the strain at failure (at the grips) was 11.2%, 16.4%, 29.3%, and 39.2%, respectively. Similar to a spring, one can trade force for displacement.
3. Aside from the core wire, no propagating transformation fronts were detected in the 1×27 cable or its multi-layered sub-components. Although some localized strain and temperature characteristics were measured by stereo digital image correlation (DIC) and infrared imaging, these features never propagated during phase transformation. The origin of this behavior was traced to pre-existing indents (contact stress concentrations) between adjacent wire layers, arising from the cable's manufacturing process. Localizations were evenly distributed along the specimen length (due to the pattern of many indents), and they slowly grew and faded according to the global elongation rate of the specimen. These observations explain why the temperature field of the 1×27 specimen from Part I was nearly uniform, giving the impression of homogeneous transformation.
4. As confirmed by post-testing inspection, no premature failure of interior wires occurred in either cable or its components. Also, little (if any) relative sliding occurred between wires during mechanical testing even when subjected to large strains (40%).
5. To further analyze the 1×27 cable, the mechanical responses of the various components were subtracted from one another, leading to the following observations:
 - (a) In the absence of a direct measurement, response subtraction provided a reasonable estimate of the mechanical behavior of each layer in the 1×27 cable.
 - (b) Unlike the 7×7 cable and core strand which exhibited clear transformation plateaus, the responses of the 1×15 and 1×27 made it difficult to discern when transformation began or ended for each layer. By comparing changes in the subtracted responses along with the DIC strain fields, it became possible to detect the start and end of transformation in the individual wire layers.
 - (c) The "stair-step" behavior of the 1×15 and 1×27 torque, which was first observed in Part I, was traced back to the layered construction of the cable. The progression in geom-

etry from inner wire layers to outer layers involves a deeper helix angle, of an alternating sign, and a larger mean helix radius. This causes inner layer wires to transform earlier than outer layer wires, resulting in the “stair-step” force and torque responses seen.

Since this is the first detailed experimental study of SMA cables to our knowledge, we conclude this article series with some comments on potential future work. Overall, the prospects for new applications of SMA cables appears bright, yet challenging. The two cable designs studied herein provide an idea of the breadth of mechanical responses offered by SMA cables, but a myriad of other possible cable cross-sections, alloy compositions, and lays remain to be explored. Faced with a multitude of options, the design engineer will need reliable modeling/computational tools to predict the behavior of new designs. This is a challenging prospect since three dimensional polycrystalline SMA constitutive models are still maturing (Lagoudas et al., 2006), and tension/torsion/bending data on (even initially straight) SMA wires are rare. Furthermore, while we focused on the superelastic behavior of these SMA cables due to their sub-ambient (stress-free) transformation temperatures, SMA cables do indeed exhibit the shape memory effect if sufficiently cooled (Reedlunn et al., 2009). SMA cables made of different NiTi alloys with elevated transformation temperatures could certainly be used as thermally-responsive, high-tension actuators. As previously mentioned in Part I, the cable form of SMAs should enable the future development of cost-effective, flexible (in bending/twisting), and highly tailorable actuators. SMA cable actuators in prosthetic limbs (Bundhoo et al., 2009), for example, could be bent around tight hinge radii and designed to give the precise force–displacement response necessary to give the prosthetic a natural feel. Future research in experiments and modeling, while demanding, would be a worthwhile endeavor, as we have as yet only scratched the surface of the potential utility of SMA cables.

Acknowledgments

We gratefully acknowledge the financial support for this work, provided by General Motors Research and Development through the GM/UM Collaborative Research Laboratory (CRL) in Smart

Materials and Structures, the National Science Foundation (CMMI-0727331), and the US Department of Energy–Office of Basic Energy Sciences (DE-SC0003996). Helpful discussions with the members of the GM/UM CRL throughout the course of this work are acknowledged. Specimen materials were provided by Fort Wayne Metals Research at not cost, along with helpful guidance from Ray Bouthot, which are also very much appreciated.

References

- Bundhoo, V., Haslam, E., Birch, B., Park, E., 2009. A shape memory alloy-based tendon-driven actuation system for biomimetic artificial fingers Part I: Design and evaluation. *Robotica* 27, 131–146.
- Chang, B.C., Shaw, J.A., Iadicola, M.A., 2006. Thermodynamics of shape memory alloy wire: modeling, experiments, and application. *Continuum Mechanics and Thermodynamics* 18, 83–118.
- Iadicola, M.A., Shaw, J.A., 2002. An experimental setup for measuring unstable thermo-mechanical behavior of shape memory alloy wire. *Journal of Intelligent Material Systems and Structures* 13, 157–166.
- Jacobus, K., Sehitoglu, H., Balzer, M., 1996. Effect of stress state on the stress-induced martensitic transformation in polycrystalline Ni–Ti alloy. *Metallurgical and Materials Transactions A* 27, 3066–3073. <http://dx.doi.org/10.1007/BF02663855>.
- Lagoudas, D., Entchev, P., Popov, P., Patoor, E., Brinson, L., Gao, X., 2006. Shape memory alloys Part II: Modeling of polycrystals. *Mechanics of Materials* 38, 430–462.
- Liu, Y., Liu, Y., Van Humbeeck, J., 1998. Lüders-like deformation associated with martensite reorientation in NiTi. *Scripta Materialia* 39, 1047–1055.
- Miyazaki, S., Otsuka, K., 1986. Deformation and transition behavior associated with the R-phase in Ti–Ni alloys. *Metallurgical and Materials Transactions A* 17, 53–63.
- Reedlunn, B., 2011. Thermomechanical Behavior of Shape Memory Alloy Cables and Tubes. Ph.D dissertation. The University of Michigan. Department of Mechanical Engineering.
- Reedlunn, B., Shaw, J.A., Daly, S., 2009. Shape memory alloy cables: exploratory experiments. *Proceedings of the Conference on Smart Materials, Adaptive Structures and Intelligent Systems SMASIS 2009*. ASME, pp. 149–160.
- Reedlunn, B., Daly, S., Shaw, J.A., accepted for publication. Superelastic shape memory alloy cables: Part I – Isothermal tension experiments. *International Journal of Solids and Structures*. <http://dx.doi.org/10.1016/j.ijsolstr.2013.03.013>.
- Shaw, J.A., Kyriakides, S., 1995. Thermomechanical aspects of NiTi. *Journal of the Mechanics and Physics of Solids* 43, 1243–1281.
- Sun, Q.P., Li, Z.Q., 2002. Phase transformation in superelastic NiTi polycrystalline micro-tubes under tension and torsion—from localization to homogeneous deformation. *International Journal of Solids and Structures* 39, 3797–3809.
- Sun, Q.P., Li, Z.Q., Tse, K.K., 2000. On superelastic deformation of NiTi shape memory alloy micro-tubes and wires – band nucleation and propagation. In: *Proceedings of IUTAM Symposium on Smart Structures and Structronic Systems*, Magdeburg Germany.